# STUDIES ON PEROVSKITE BASED PHOTOVOLTAIC DEVICES

**Pre-PhD Seminar by**

Paramesh Chandra

**Registration No –** VB-679 of 2015-16

**Supervisor:** Swapan Kumar Mandal

**5th April 2023**

# Presentation Arrangement

- Introduction
- Methods and Instrumentation
- Sample preparation and device fabrication
  - $CH_3NH_3Cl$ sample preparation
  - $(CH_3NH_3)_3Bi_2Cl_9$ sample preparation
  - Device fabrication
- Results and Discussion
  - Morphology controlled $(CH_3NH_3)_3Bi_2Cl_9$ thin film for lead free perovskite solar cell
  - A dielectric study of Br-doped lead-free methylammonium bismuth chloride $(CH_3NH_3)_3Bi_2Br_xCl_{9-x}$
  - Frequency and temperature dependent dielectric characteristics of lead free Br doped perovskite $(CH_3NH_3)_3Bi_2Cl_9$ and $(CH_3NH_3)_3Bi_2Br_xCl_{9-x}$
  - Observation of negative photoconductivity in $(CH_3NH_3)_3Bi_2(Br_xCl_{1-x})_9$: correlating ion-migration, instability and efficiency in halide perovskite solar cell
- Conclusions
- Arrangement of Thesis
- List of publications
- Acknowledgement

# What is perovskite based photovoltaics?
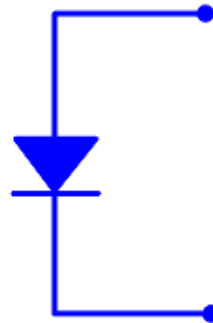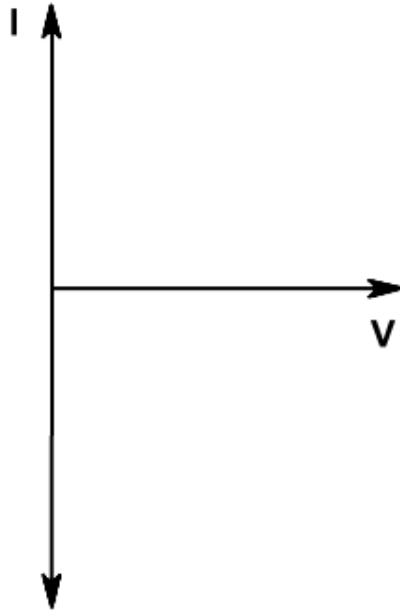
## What is perovskite?

## What is photovoltaics?

**A device that converts solar energy to electrical energy**
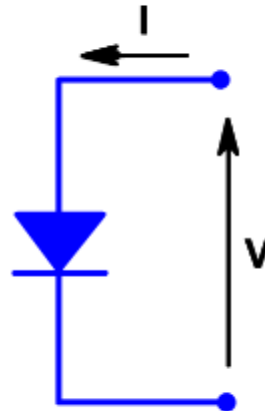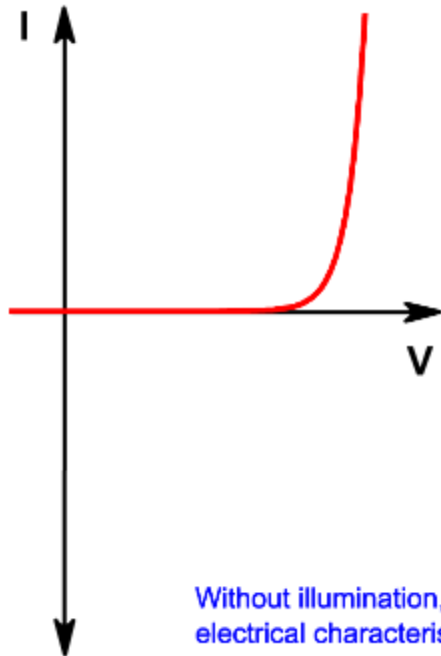
## Solar cell model

The I-V curve of a solar cell is the superposition of the I-V curve of the solar cell diode in the dark with the light-generated current. The light shifts the I-V curve down into the fourth quadrant, where power can be extracted from the diode. Illuminating a cell adds to the normal "dark" currents in the diode so that the diode law becomes:

$$I = I_0 \left[ \exp(\frac{qV}{nkT}) - 1 \right] - I_L$$

where $I_L$ = light-generated current

## Solar cell model



Without illumination, a solar cell has the same electrical characteristics as a large diode.
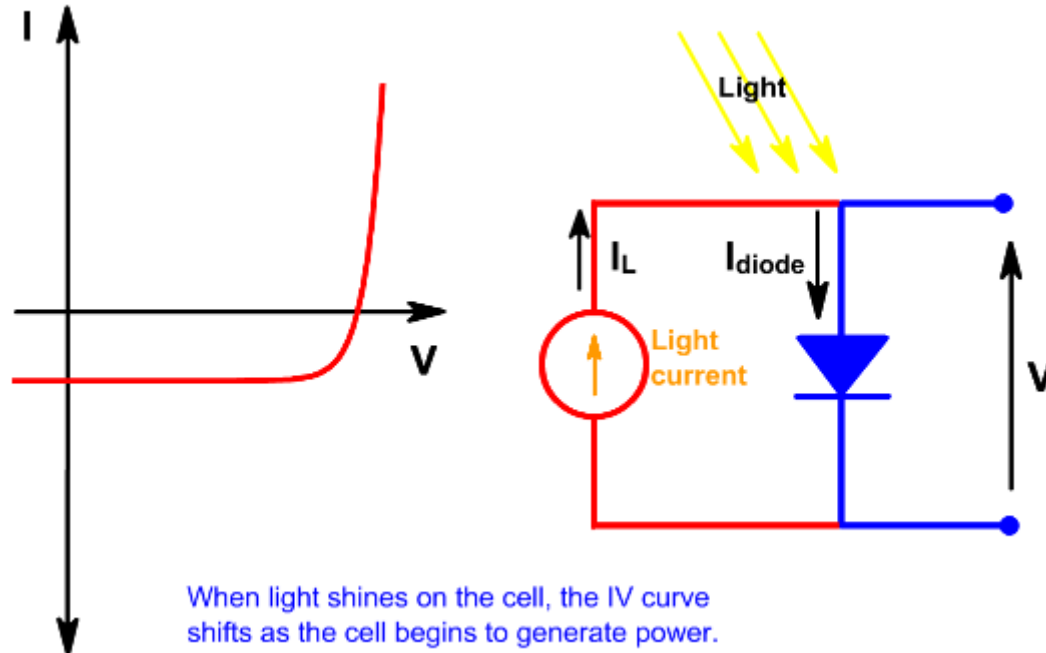
The I-V curve of a solar cell is the superposition of the I-V curve of the solar cell diode in the dark with the light-generated current. The light shifts the I-V curve down into the fourth quadrant, where power can be extracted from the diode. Illuminating a cell adds to the normal "dark" currents in the diode so that the diode law becomes:

$$I = I_0 \left[ \exp\left(\frac{qV}{nkT}\right) - 1 \right] - I_L$$

where $I_L$ = light-generated current
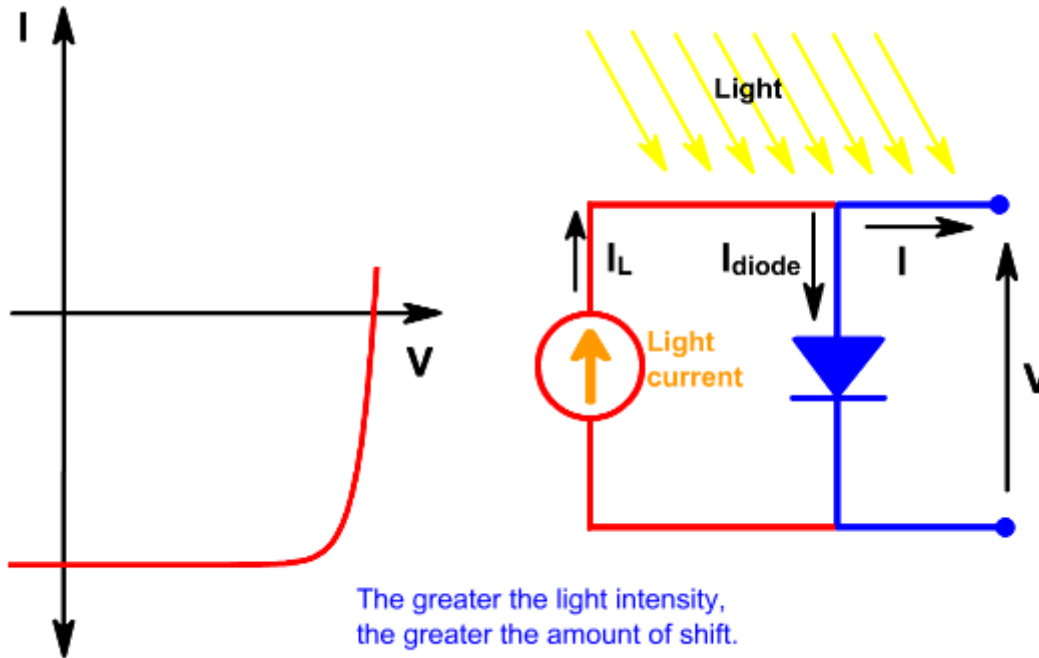
## Solar cell model

The I-V curve of a solar cell is the superposition of the I-V curve of the solar cell diode in the dark with the light-generated current. The light shifts the I-V curve down into the fourth quadrant, where power can be extracted from the diode. Illuminating a cell adds to the normal "dark" currents in the diode so that the diode law becomes:

$$I = I_0 \left[\exp(\frac{qV}{nkT}) - 1\right] - I_L$$

where $I_L$ = light-generated current

When light shines on the cell, the IV curve shifts as the cell begins to generate power.

## Solar cell model



I_L

I_diode

I

Light current

Light

The greater the light intensity, the greater the amount of shift.
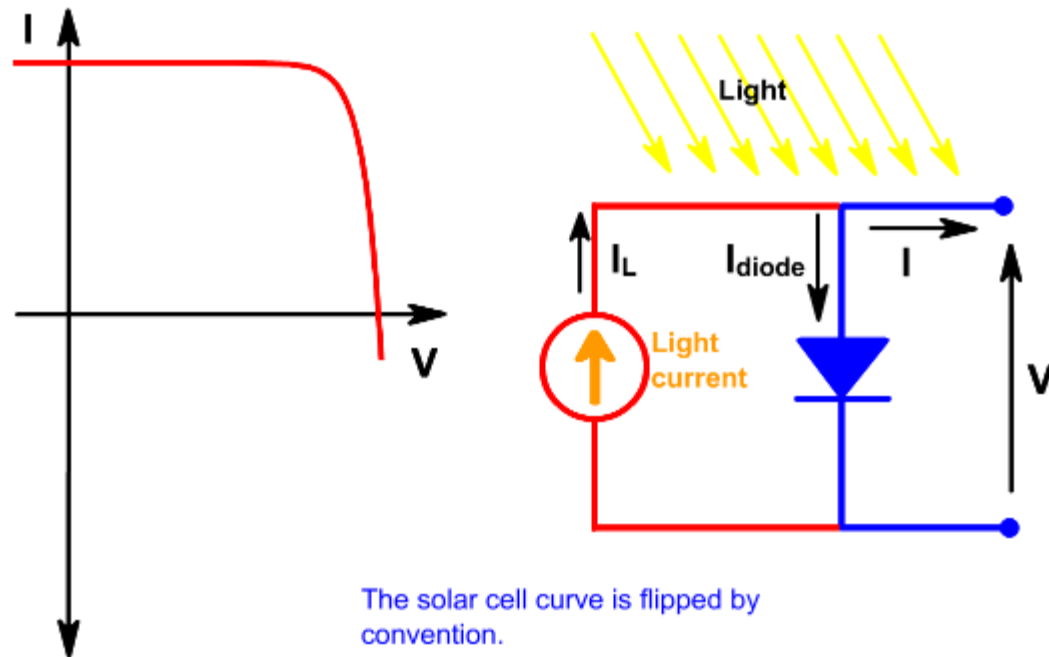
The I-V curve of a solar cell is the superposition of the I-V curve of the solar cell diode in the dark with the light-generated current. The light shifts the I-V curve down into the fourth quadrant, where power can be extracted from the diode. Illuminating a cell adds to the normal "dark" currents in the diode so that the diode law becomes:

$$I = I_0 \left[ \exp(\frac{qV}{nkT}) - 1 \right] - I_L$$

where $I_L$ = light-generated current

## Solar cell model



The solar cell curve is flipped by convention.

The I-V curve of a solar cell is the superposition of the I-V curve of the solar cell diode in the dark with the light-generated current. The light shifts the I-V curve down into the fourth quadrant, where power can be extracted from the diode. Illuminating a cell adds to the normal "dark" currents in the diode so that the diode law becomes:

$$I = I_0 \left[ \exp\left(\frac{qV}{nkT}\right) - 1 \right] - I_L$$

where $I_L$ = light-generated current

# Solar cell parameters

**Solar Cell Efficiency**

- Efficiency is the most commonly used parameter to compare the performance of one solar cell to another.
- Efficiency is defined as the ratio of energy output from the solar cell to input energy from the sun. The efficiency of a solar cell is determined as the fraction of incident power that is converted to electricity and is defined as:

$$P_{max} = V_{OC}I_{SC}FF$$
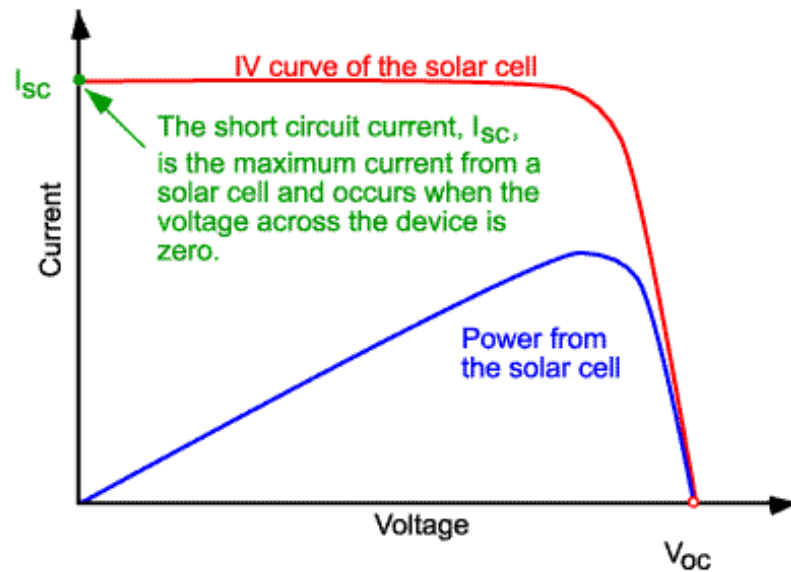
$$\eta = \frac{V_{OC}I_{SC}FF}{P_{in}}$$

Where:

$V_{oc}$ is the open-circuit voltage;

$I_{sc}$ is the short-circuit current;

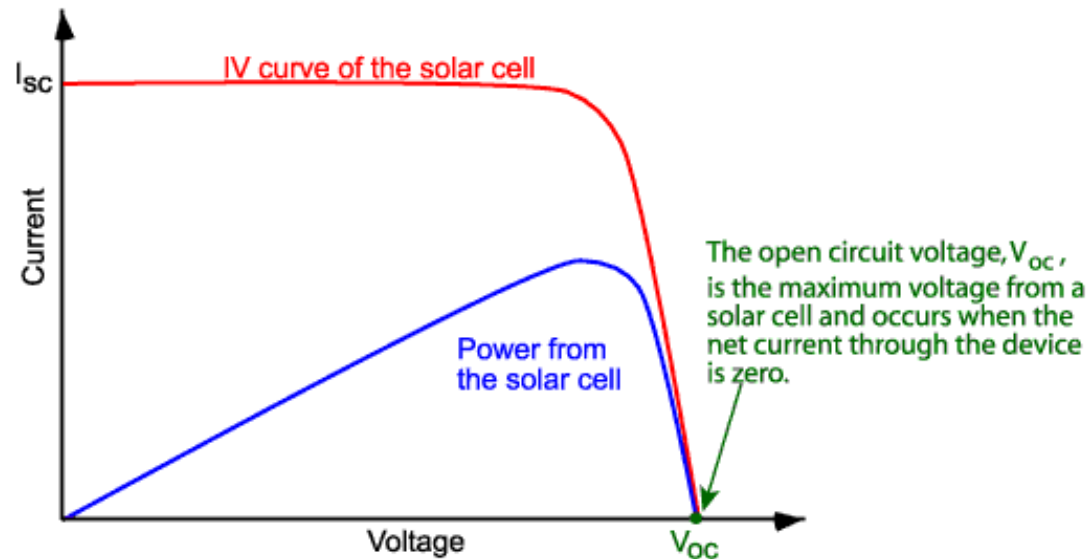$FF$ is the fill factor and

$\eta$ is the efficiency.

## Short-Circuit current



- The short-circuit current is the current through the solar cell when the voltage across the solar cell is zero (i.e., when the solar cell is short-circuited).

- Usually written as $I_{SC}$, the short-circuit current is shown on the IV curve.

## Open-circuit voltage



IV curve of the solar cell

$I_{sc}$

Current

Power from the solar cell

The open circuit voltage, $V_{OC}$, is the maximum voltage from a solar cell and occurs when the net current through the device is zero.

Voltage

$V_{OC}$

- The open-circuit voltage, $V_{OC}$, is the maximum voltage available from a solar cell, and this occurs at zero current.

- The open-circuit voltage corresponds to the amount of forward bias on the solar cell due to the bias of the solar cell junction with the light-generated current.

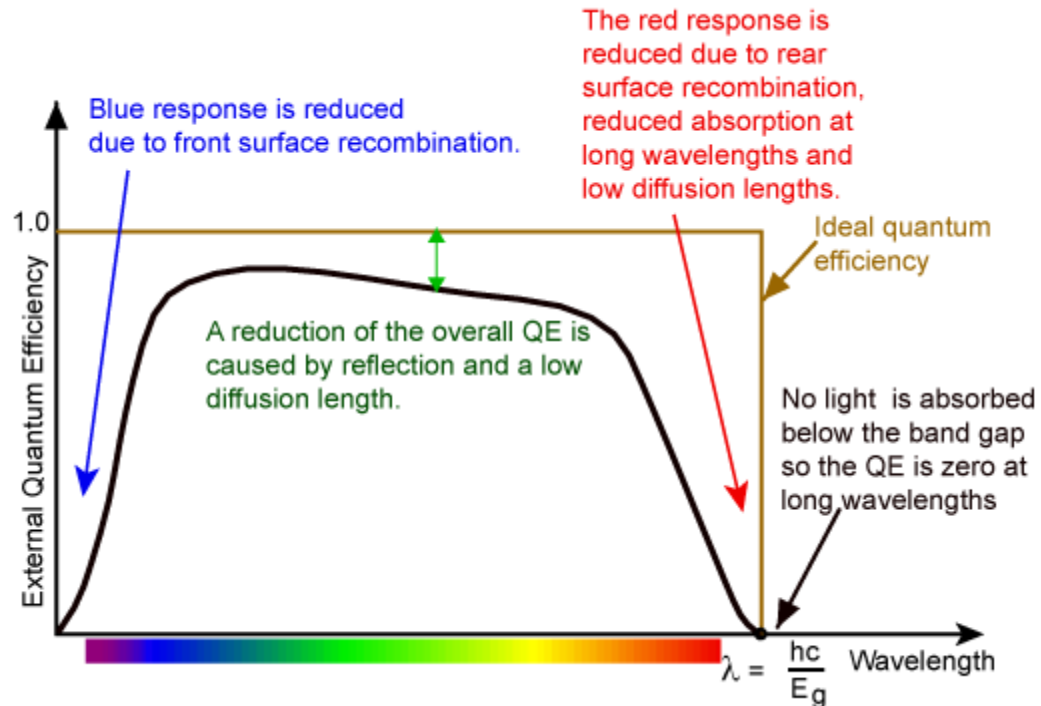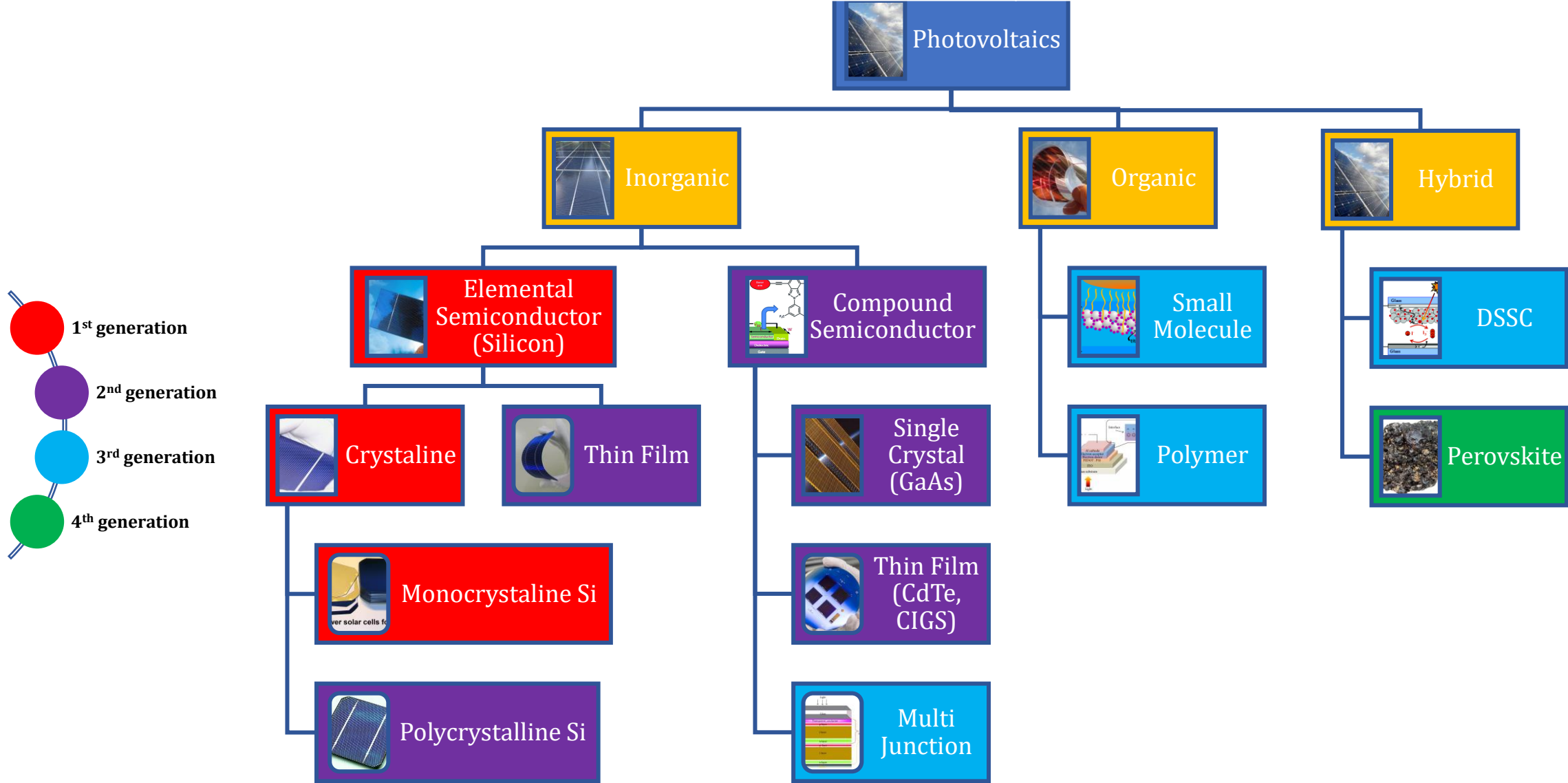$$V_{OC} = \frac{nkT}{q} \ln(\frac{I_L}{I_0} + 1)$$

## Fill factor
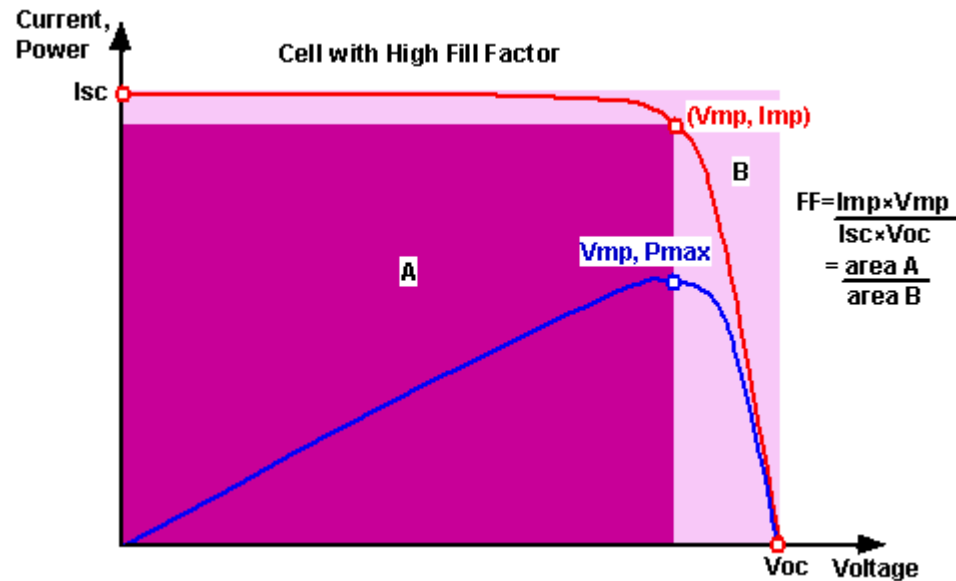


- The "fill factor", more commonly known by its abbreviation "FF", is a parameter which, in conjunction with $V_{oc}$ and $I_{sc}$, determines the maximum power from a solar cell.

- The FF is defined as the ratio of the maximum power from the solar cell to the product of $V_{oc}$ and $I_{sc}$ so that:

$$FF = \frac{P_{MP}}{V_{OC} \times I_{SC}} = \frac{V_{MP} \times I_{MP}}{V_{OC} \times I_{SC}}$$
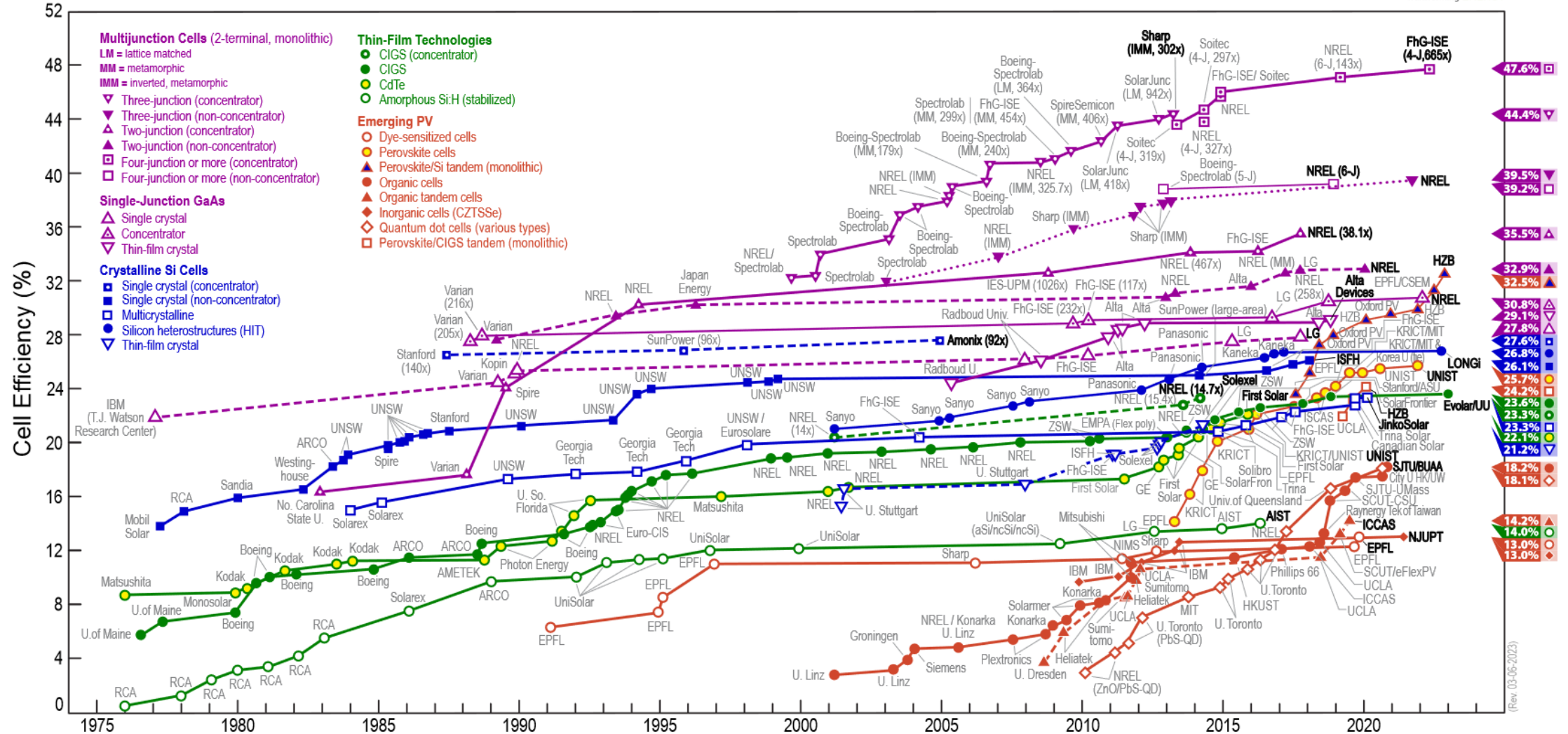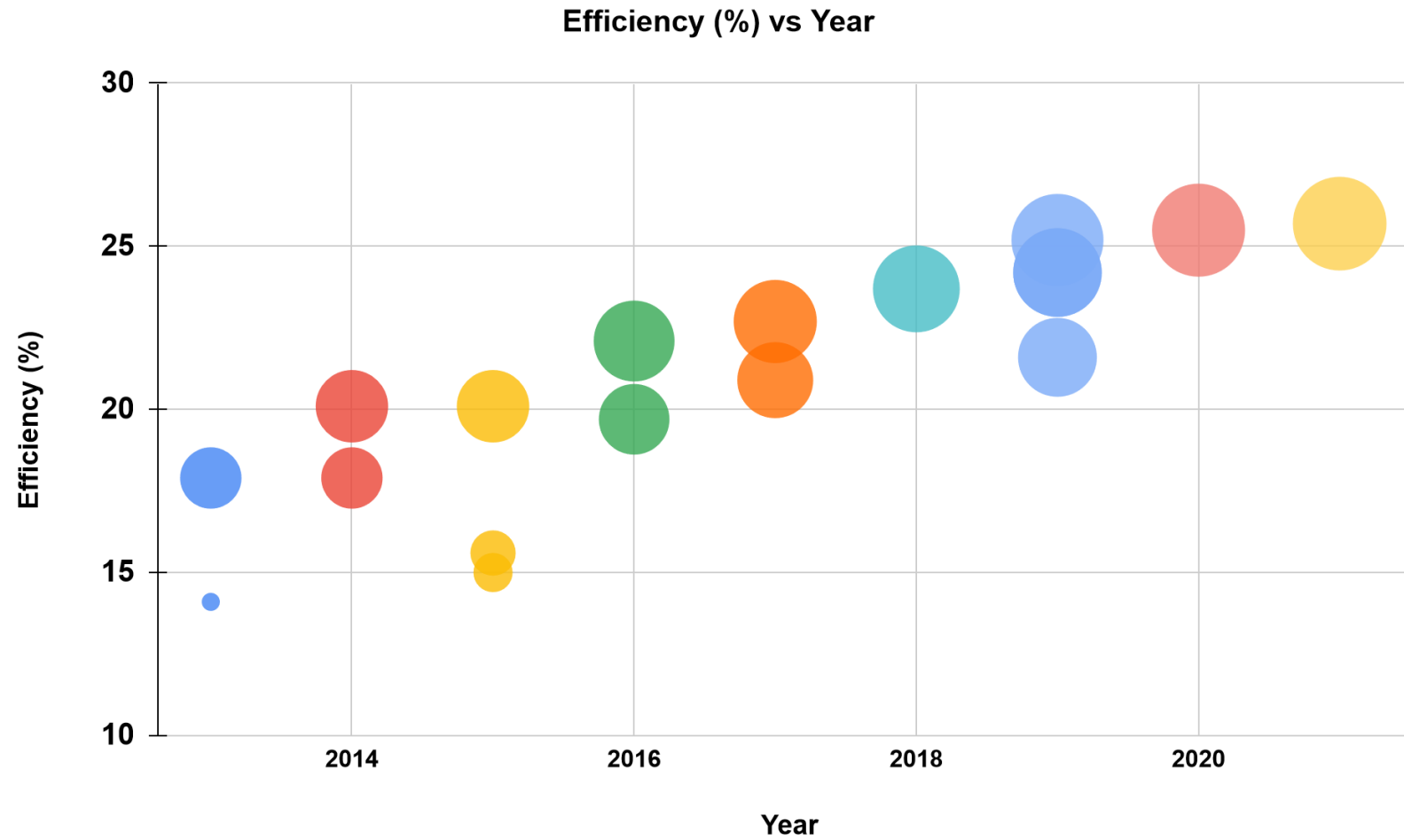
## Quantum efficiency



- The "quantum efficiency" (Q.E.) is the ratio of the number of carriers collected by the solar cell to the number of photons of a given energy incident on the solar cell.

- The quantum efficiency may be given as a function of wavelength or energy. If all photons of a certain wavelength are absorbed, and the resulting minority carriers are collected, then the quantum efficiency at that particular wavelength is unity.

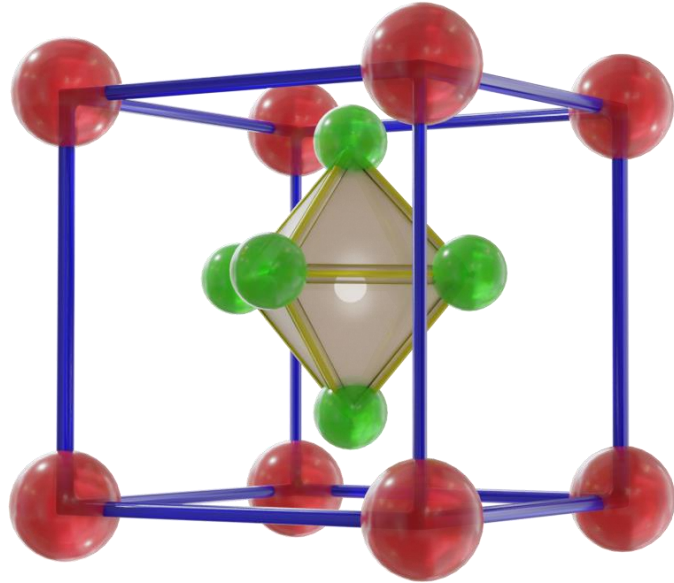- The quantum efficiency for photons with energy below the band gap is zero.

Photovoltaics

Inorganic

Organic

Hybrid

1st generation

2nd generation

3rd generation

4th generation

Elemental Semiconductor (Silicon)

Compound Semiconductor

Small Molecule

DSSC

Crystaline

Thin Film

Single Crystal (GaAs)

Polymer

Perovskite

Monocrystaline Si

Thin Film (CdTe, CIGS)

Polycrystalline Si

Multi Junction

Best Research-Cell Efficiencies — NREL

## Perovskite efficiency table



Efficiency (%) vs Year

- Perovskite derives its name from the mineral structure Calcium Titanium oxide, discovered by German mineralogist Gustav Rose in 1839.

- The special structure of this mineral was later characterized by Russian mineralogist Lev. A. perovski, thus the name.

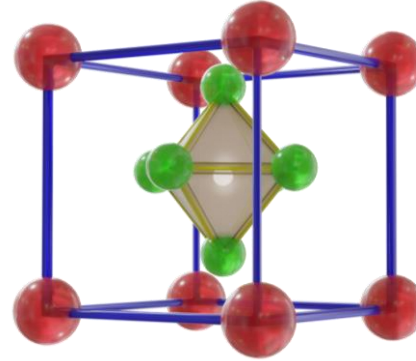- Chemical formula of perovskite in $ABX_3$

**A** = Cation

**B** = Metal ion

**X** = Anions as Oxygen, Halogens, or alkali metals

**Some properties of perovskites**

**Some features of perovskites**

- Perovskite ideally has a cubic structure, but due to temperature, it also shows tetragonal, octahedral, and orthorhombic structures.

- Electrical properties governed by mostly the B-X bond, which are in most cases inorganics

- A cation does not participate in electronic properties.



- Easy fabrication methods

- Small and tuneable bandgap

- High extinction coefficient

- High carrier mobility

**Features of perovskite with numbers**

| | |
|---|---|
| **Bandgap** | • Direct bandgap of 1.55 eV |
| **Binding energy of excitation** | • Small (~ 0.030 eV) |
| **Carrier mobility** | • High (7.5 cm$^2$/V.s for electron and 12.5 cm$^2$/V.s for holes |
| Charge diffusion length | • Large (ranging from 100-1000 nm) |
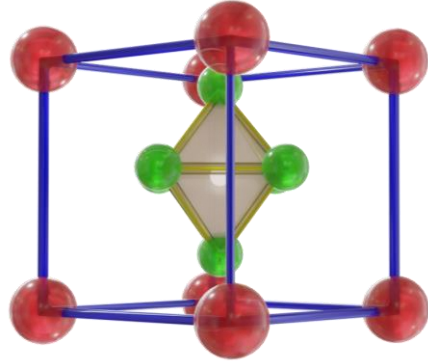
**Organometal halide perovskite as visible light sensitizer for photovoltaic cell**

Akhihiro Kojima, Keshima Teshima, Yasuo Shirai & Tsutomu Miyasaka.

*J. Am. Chem. Soc.* 2009, 131, 17, 6050–6051

- The hybrid perovskite made its debut in photovoltaic in 2006 when Miyasaka and group employed $CH_3NH_3PbBr_3$ as a sensitizer on nanoporous $TiO_2$ in liquid electrolyte-based dye-sensitized solar cell (DSSC) realising efficiency of 2.2 %

**Efficiency = 3.8 %**

**$V_{OC}$ = 0.96 V**

**EQE = 65 %**
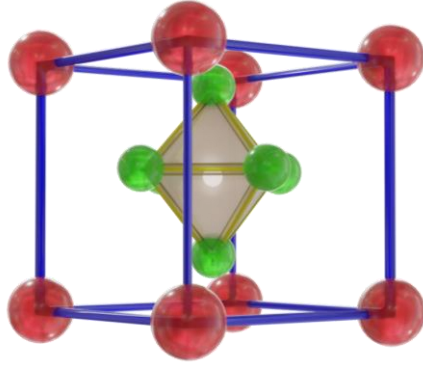
**Efficiency = 10.9 %**

$V_{OC}$ = 1.1 V

**Efficient hybrid solar cell based on meso-superstructured organometal halide perovskite**

Michael M. Lee, Joel Teuscher, Tsutomu Miyasaya, Henr J. Snaith

Science vol 338 2 November 2012

- They fabricated solution-processable solar cells using mesoporous $TiO_2$ as the transparent n-type component, & spiro-oMeTAD as the transparent p-type hole conductor with PCE, ~ 8 %.

- They also found that the replacement of mesoporous n-type $TiO_2$ with insulating $Al_2O_3$ improved the power conversion efficiency by up to 10.9%.
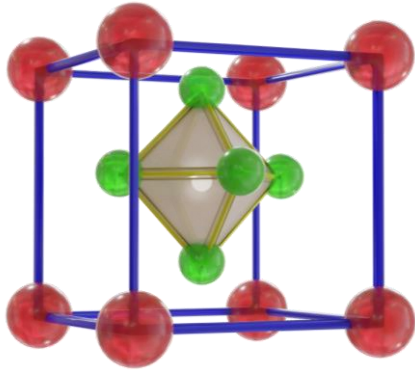
**Efficiency = 12 %**

**Electron hole diffusion length exceeding 1 micrometre in an organic trihalide perovskite absorber**

Samuel D, Stranks, HenryJ. Snaith *et al.*

Science vol 18 October 2013

- Comparative study of perovskite $CH_3NH_3PbI_{3-x}Cl_x$ and $CH_3NH_3PbI_3$ is performed

- It was found that PCEs of $CH_3NH_3PbI_{3-x}Cl_x$ are much more than $CH_3NH_3PbI_3$ (~12% and 4% respectively)

- Also found that a thick layer (~500nm) of Cl-doped lead-based perovskite is preferable over pristine Pb-based perovskite with layer thickness around (~140 nm)
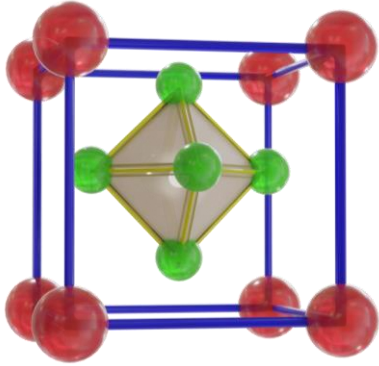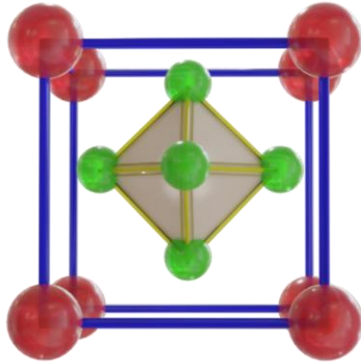
**Efficiency = 19.3 %**

**Interface engineering of highly efficient perovskite solar cells**

Huanping Zhou, Yang Yang *et al.*

Science vol 345,542 August 2014

- In this work, Yang's group used ITO (Indium doped tin oxide) & a poly-ethyleneimine ethoxylate (PEIE) was used as electrodes, Yttrium doped $TiO_2$ (Y-$Tio_2$) was used as ETL & for HTL, cobalt and lithium co-doped spiro-OMeTAD and gold as an electrode which gives the efficiency of ~ 19.3 %

- The fabrication of PSC was conducted in air and from solution at low temperatures, which should simplify the manufacturing of inexpensive large-area perovskite devices that are performed at a high level.
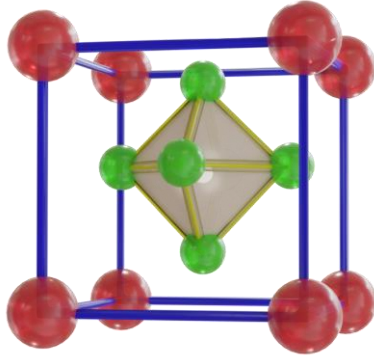
**Efficiency = 17.91 %**

**The optoelectronic role of chlorine in $CH_3NH_3PbI_3(Cl)$ – based perovskite solar cells**

Qi Chen, Yang Yang *et al.*

Nature Communications 6:7269 12 Jun 2015

- The optoelectronic properties of the prototypical $CH_3NH_3PbI_3$ can be adjusted by introducing other extrinsic ions. Specifically, chlorine incorporation has been shown to affect the morphological development of perovksite films.

- The chlorine incorporation is found to mainly improve the carrier transport across the heterojunction interfaces, rather than within the perovskite crystals. Further optimization according this protocol leads to solar cells achieving power conversion efficiency of 17.91%.
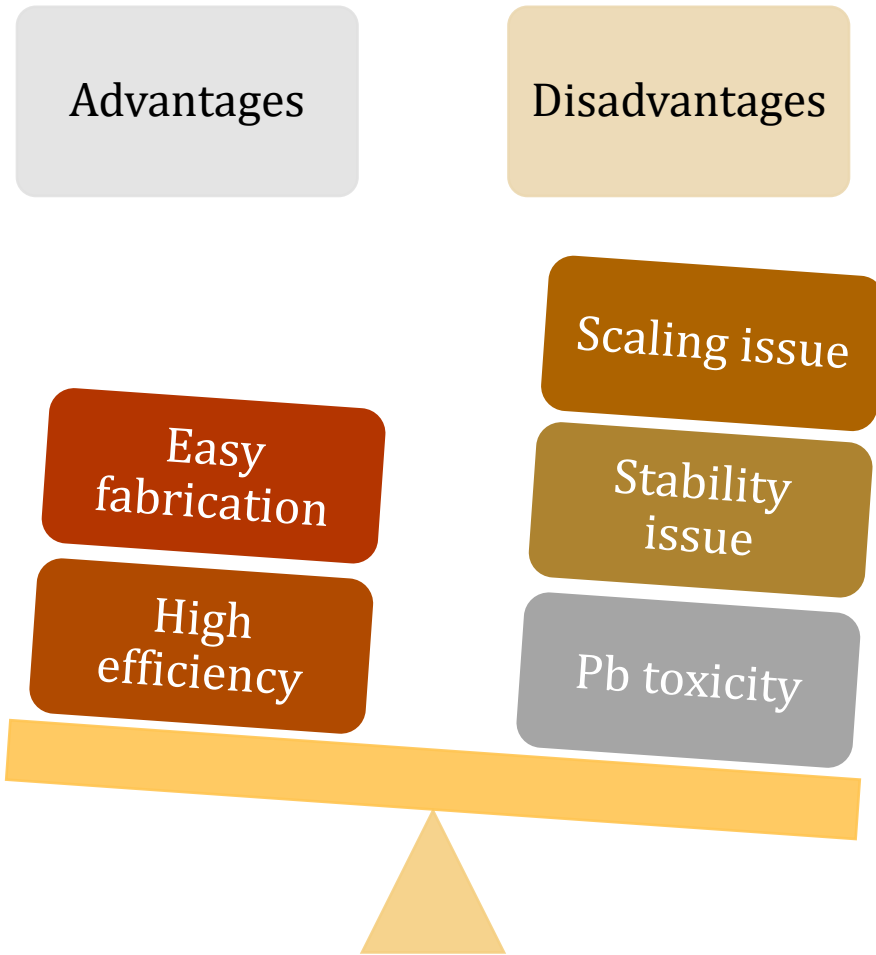
**Efficiency = 25.3 %**

**One-stone-for-two-birds strategy to attain beyond 25% perovskite solar cells**

Tinghuan Yang *et al*

[Nature Communications](#) **volume 14**, Article number: 839 (2023)

- Here, they report a one-stone-for-two-birds strategy in which both anion-fixation and associated undercoordinated-Pb passivation are in situ achieved.
- The resultant devices attain a power conversion efficiency of 25.3% (certified at 24.8%) with substantially improved stability.
- Moreover, the device without encapsulation retained 92% of its initial efficiency after 5000 h exposure to ambient conditions.

**Why is perovskite still not commercialized?**

Advantages

Disadvantages

Scaling issue

Easy fabrication

Stability issue

High efficiency

Pb toxicity

- Pb toxicity
- Stability issue
- Scaling issue

## Objectives

- In our work focuses on replacing Pb with another nontoxic metal ion.

- Tweak the disposition technique to make the cells more efficient.

- Try to find some intrinsic properties of perovskites and the reason behind their low efficiency.

- Replace HTL with other low-cost materials.

## Why have we chosen Bi in place of Pb?



**[Xe]** $(4f^{14}5d^{10}6s^26p^2)$

**[Xe]** $(4f^{14}5d^{10}6s^26p^3)$

- Defect-tolerant perovskite structure could be replicated in materials with heavy metal cation with a stable pair of valence s electrons.

- This is why we have considered bismuth ($Bi^{3+}$) (electron configuration of $Bi^{3+}$ and $Pb^{2+}$ is similar.

- $Bi^{3+}$ being a heavy metal cation, band dispersion due to spin-orbit coupling is expected.

- High dielectric constants that are important for increased screening of charged defects.

- Also, the low toxicity of bismuth and lack of exploration of this field makes it a desirable topic for solar cell researchers.

# Methods we have used
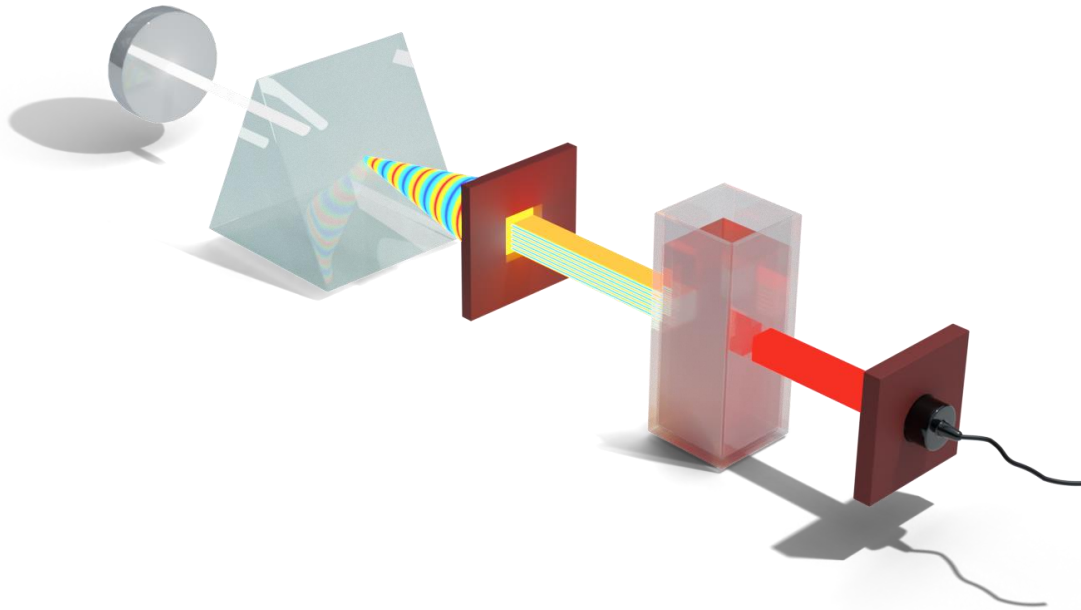
## UV –Vis spectroscopy



**Fig 1.** UV-Vis measurement setup schematic diagram

- UV-Vis spectroscopy measurement setup is used to determine the absorption spectrum of the sample prepared.

- From the absorption spectrum, we have determined the band gap.

- Optical properties were measured with Beckman Coulter DU720 UV-Vis spectrometer in our lab.
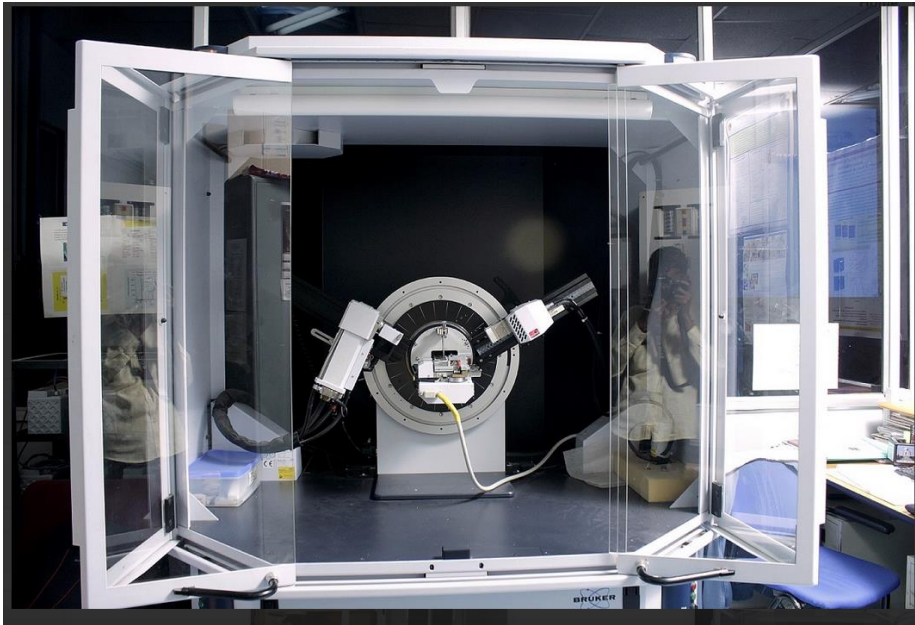
## X-ray diffraction study



Fig 2. XRD measurement setup

- X-ray crystallography is used to measure the bond distances between the metal and the ligands.
- It also gives the information about the changes in the lattice parameters.
- It is also possible to ascertain from such data structural details such as space group by application of Rietveld Method.
- Powder XRD system with 1D PSD (Bruket LynxEye)

## Scanning electron microscopy (SEM)



**Fig 3**. SEM setup and schematic diagram of the measurement process
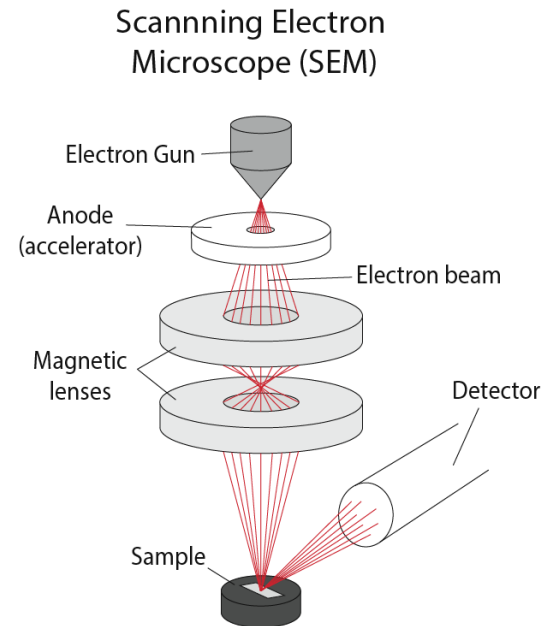
- SEM is extensively used to study films and powder sample morphology.
- EDAX system determines the atomic percentage of different atomic species.
- ZEISS GeminiSEM 450 is used for the study provided by Visva-Bharati.

## IV – characterization unit



**Fig 4.** I-V characterization unit

- Keithlay 6514 source meter is used for the current measurement
- Arduino-based voltage source is used to automate the process.
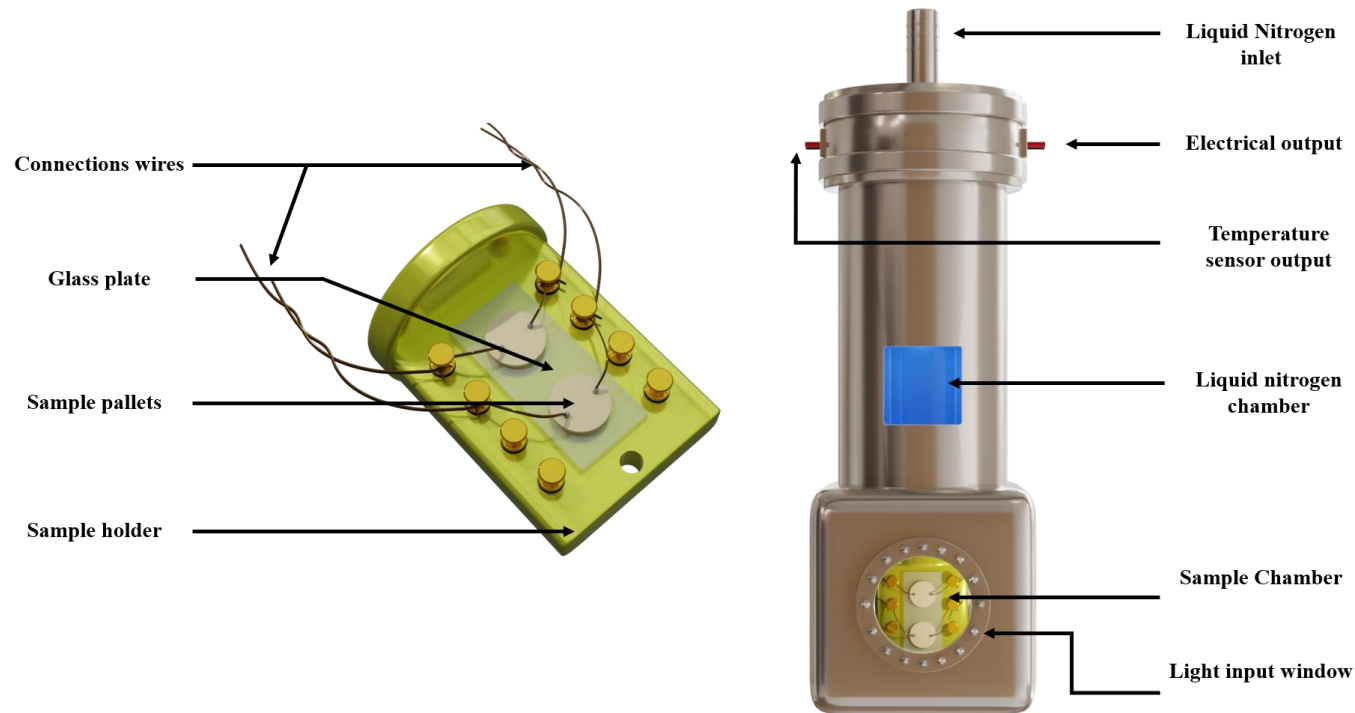- I-V measurement is automated using a python interface, and the code is written by us.

## Dielectric characterization unit





Electrodes

Sample
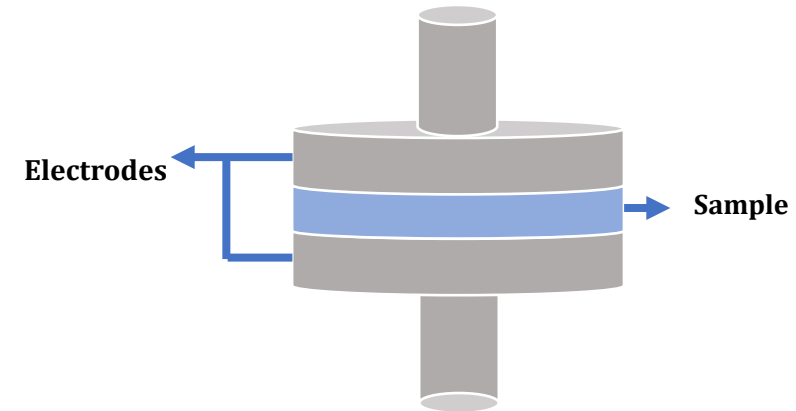
- Dielectric measurement setup with variable temperature range 100 K – 500 K.
- UGC-CSR Indore provided this facility.

**Fig 5.** Dielectric measurement setup with cryo facility.

## Cryo measurement probe



Connections wires

Glass plate

Sample pallets

Sample holder

Liquid Nitrogen inlet

Electrical output

Temperature sensor output

Liquid nitrogen chamber

Sample Chamber

Light input window

- Lab-made setup to measure I-V and I-t properties of the sample pallets using different kinds of biasing condition
  - Photo bias
  - External electric field bias
  - Temperature bias
  - Can be upgraded to include more
- External voltage supply and source meter is controlled using a python interface.

**Fig 6.** Cryo multi-purpose measurement setup

## Light stability measurement setup



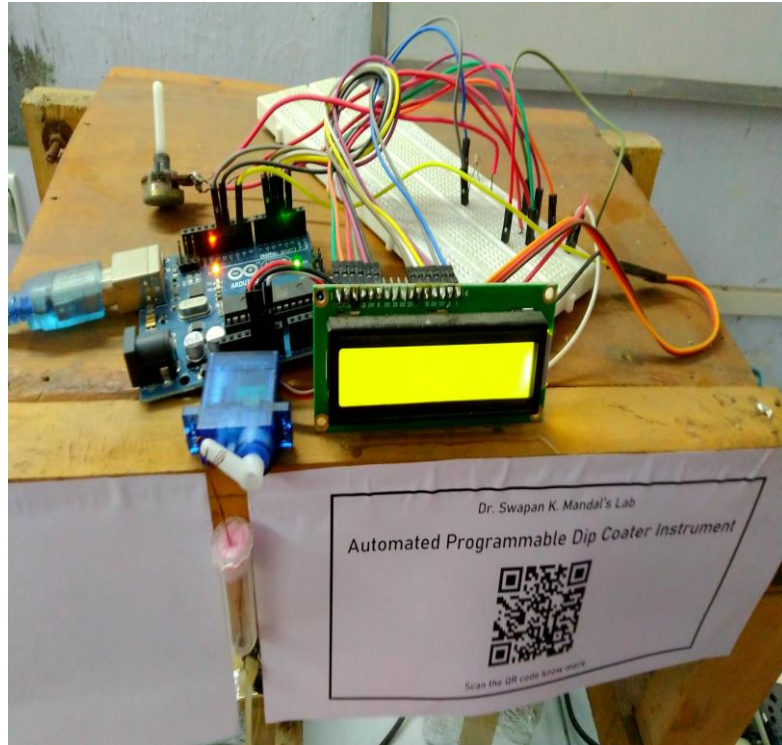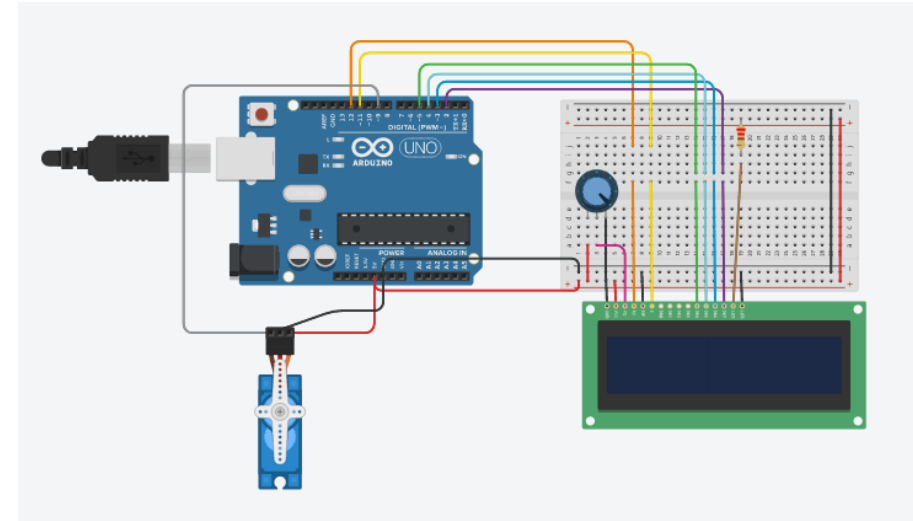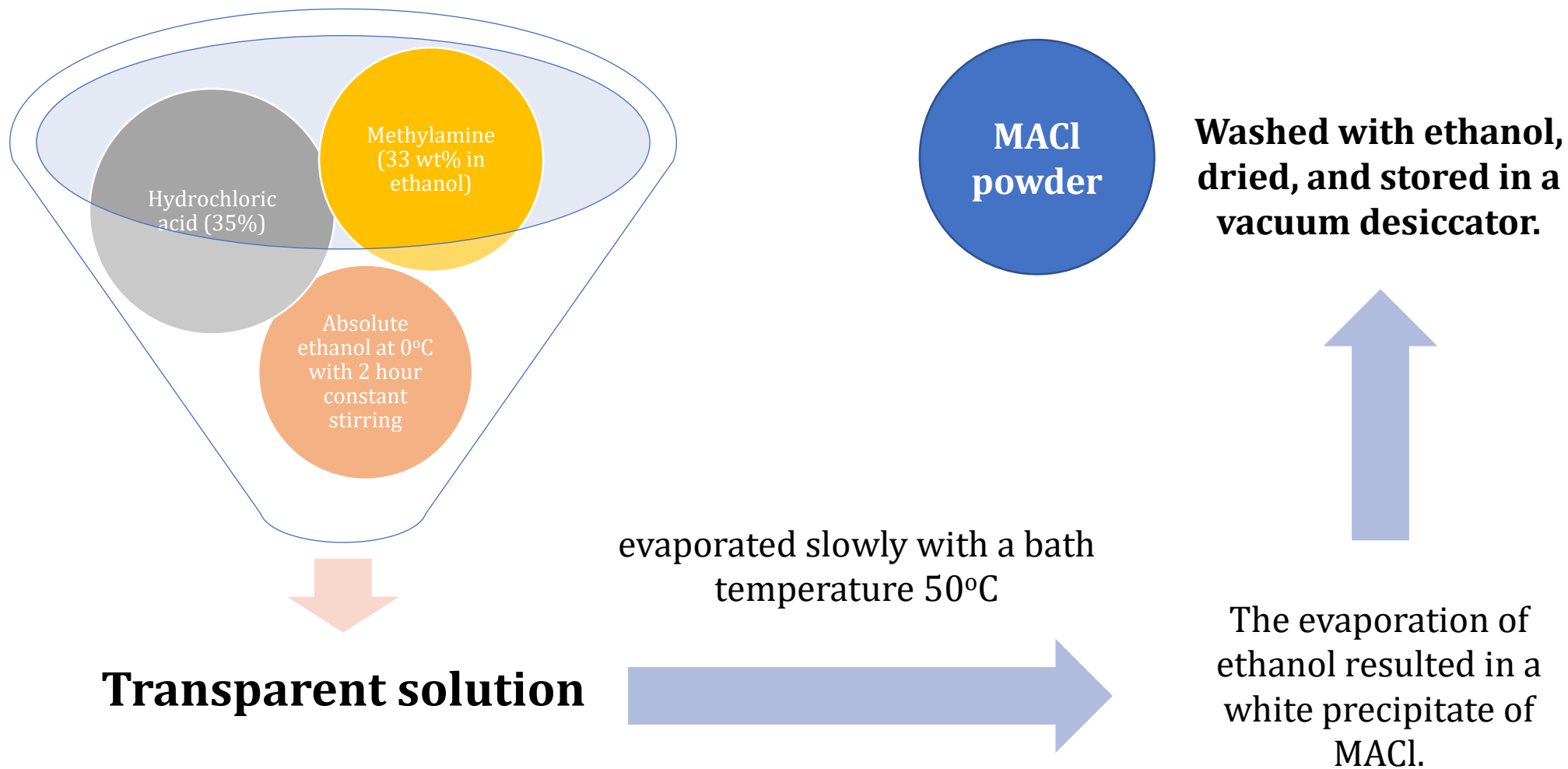**Fig 7.** Automated stability measurement setup under low temperature

## Dip coating setup


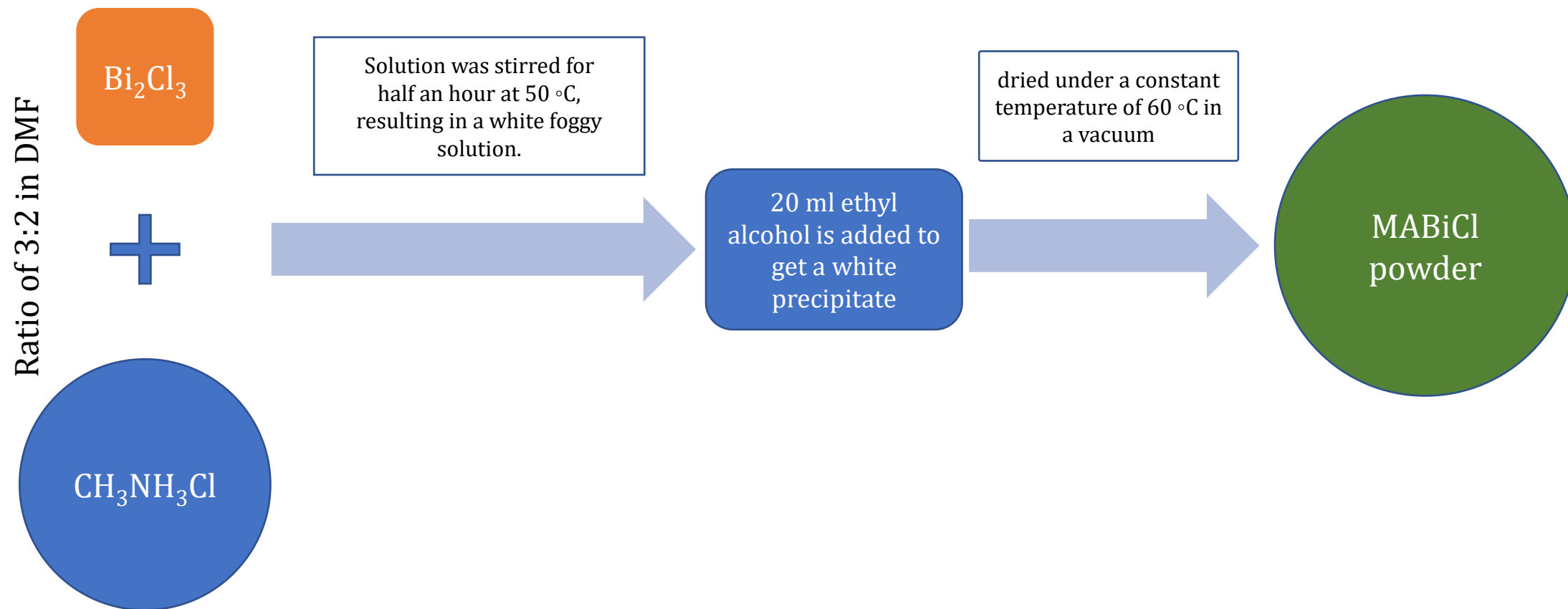


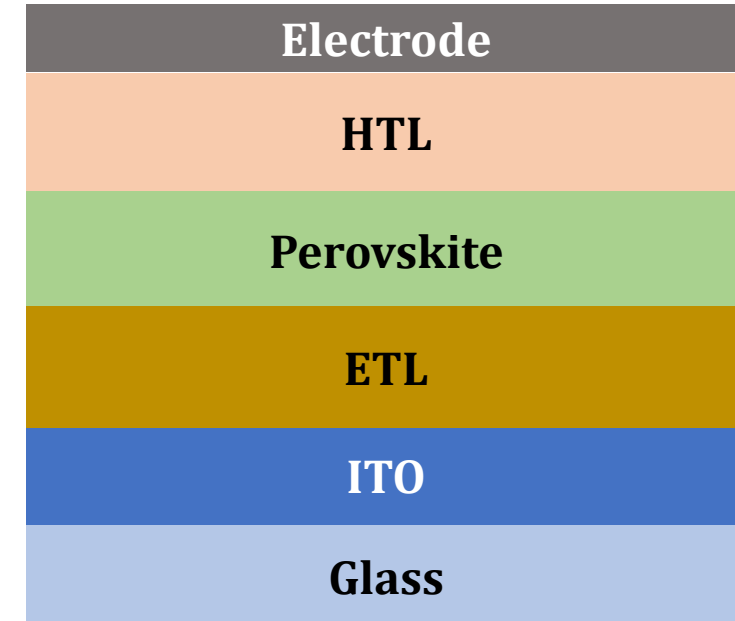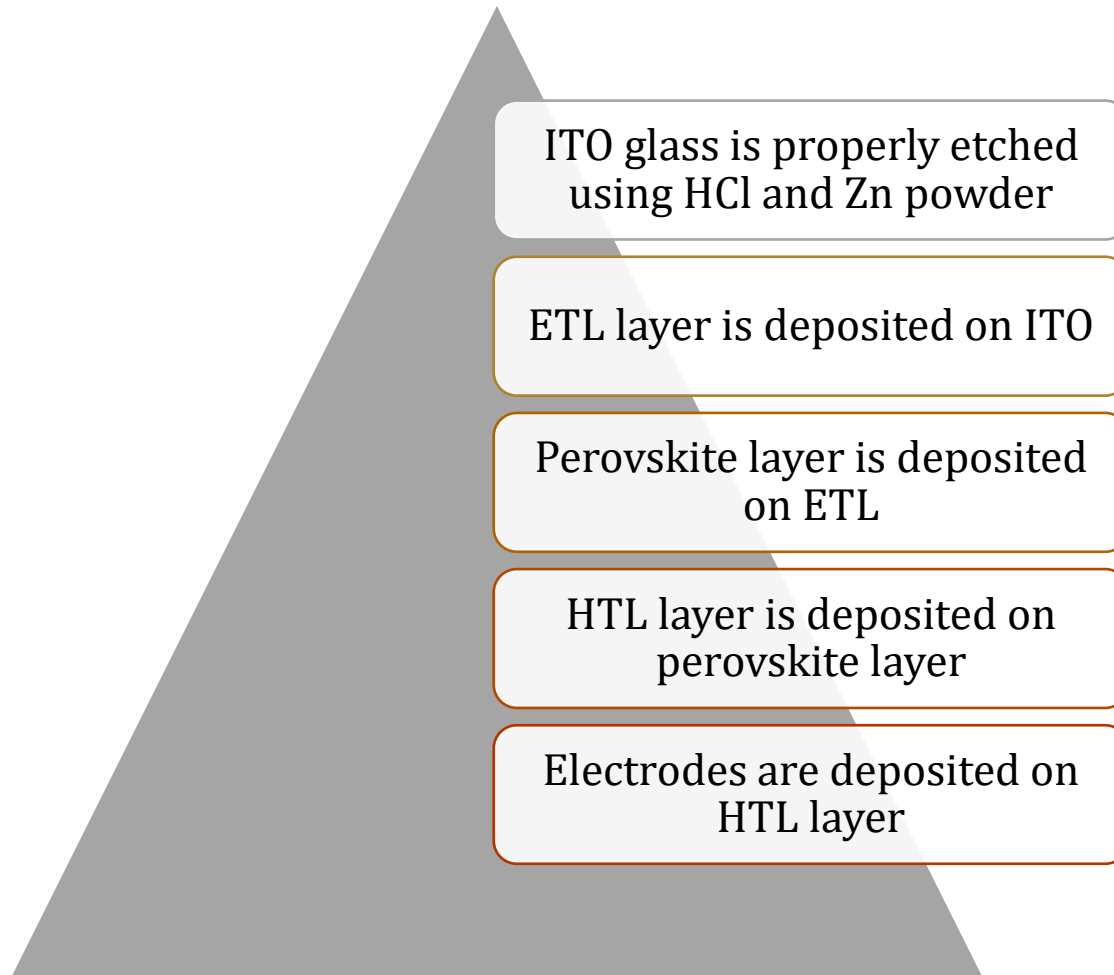**Fig 8.** Arduino-based dip coating setup

- Lab-made dip coater unit using Arduino and Servo motors.

- Dip coating speed can be as low as 0.1 mm/sec.

- After every dip, the substrate is dried with hot air flow.

# Sample preparation and solar cell fabrication

Hydrochloric acid (35%)

Methylamine (33 wt% in ethanol)

Absolute ethanol at 0°C with 2 hour constant stirring

**Transparent solution**

evaporated slowly with a bath temperature 50°C

The evaporation of ethanol resulted in a white precipitate of MACl.

**MACl powder**

**Washed with ethanol, dried, and stored in a vacuum desiccator.**

Ratio of 3:2 in DMF

$Bi_2Cl_3$

+

$CH_3NH_3Cl$

Solution was stirred for half an hour at 50 ◦C, resulting in a white foggy solution.

20 ml ethyl alcohol is added to get a white precipitate

dried under a constant temperature of 60 ◦C in a vacuum

MABiCl powder

ITO glass is properly etched using HCl and Zn powder

ETL layer is deposited on ITO

Perovskite layer is deposited on ETL

HTL layer is deposited on perovskite layer

Electrodes are deposited on HTL layer

| Electrode |
|---|
| **HTL** |
| **Perovskite** |
| **ETL** |
| **ITO** |
| **Glass** |

# Morphology controlled $(CH_3NH_3)_3Bi_2Cl_9$ thin film for lead free perovskite solar cell

**Fig 9.** Schematic diagram of the fabricated solar cell device structure

- ITO-coated glass substrates (1 cm x 1 cm) were etched to obtain the required pattern for device fabrication.
- ITO glasses were further cleaned with deionized water, and ethanol using an ultrasonicator and finally dried.
- A compact layer of $TiO_2$ was deposited using a **dip-coating method**.
- The substrate was annealed at $450^oC$ for 1 hr.
- $TiO_2$ coated substrate was again coated with MABiCl.
- The whole system of layers is kept at $100^oC$ for 30 minutes.
- After that, another ITO glass is attached to the top of the MABiCl layer using the silver paste as the contact layer.
- The whole device is annealed at $100^oC$ for 30 minutes to finalize the process.
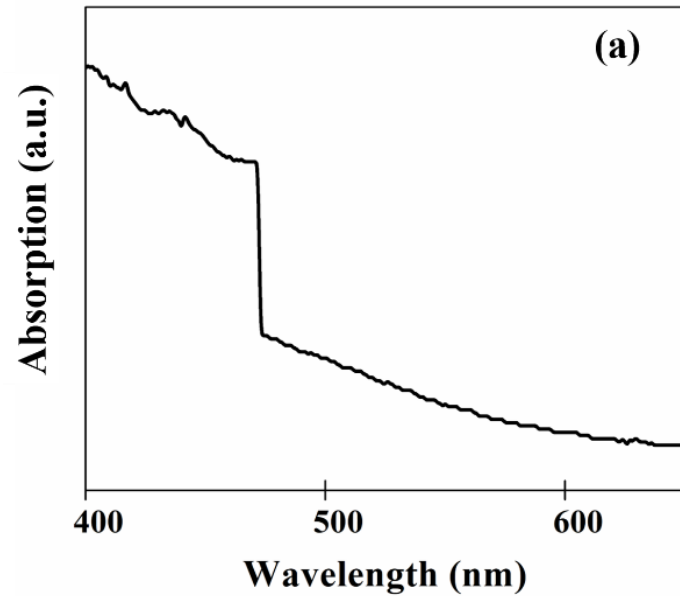
**Fig 10.** Optical absorption spectra of MABiCl perovskite

- The optical band gap of the semiconducting nanostructure was determined using Taucs' plot by plotting $(\alpha h\nu)^2$ vs. $h\nu$.

- The calculated bandgap of the perovskite thin film is found to be **2.58 eV** which is very close to the reported value of 2.51 eV.
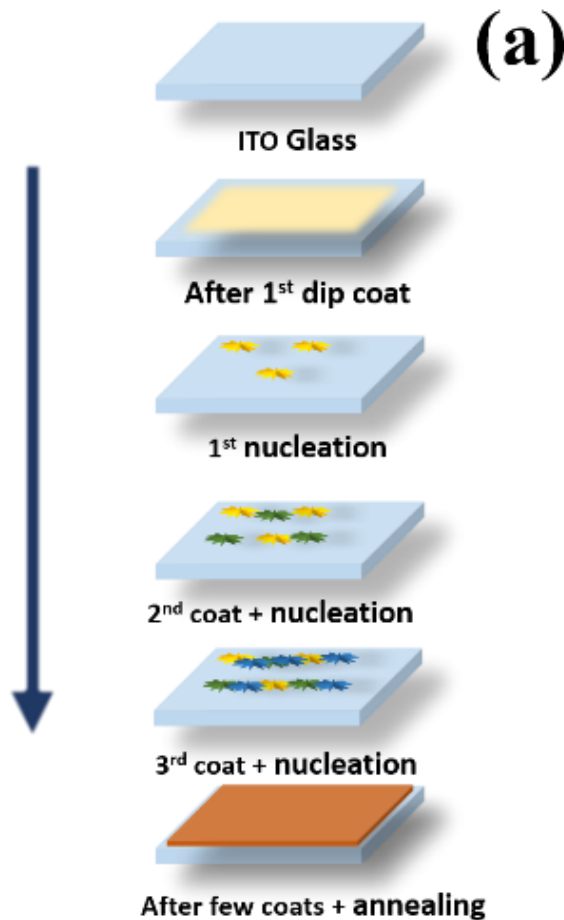
**(a)**

ITO Glass

After 1st dip coat

1st nucleation

2nd coat + nucleation

3rd coat + nucleation

After few coats + annealing



**(b)**

**Fig 11.** Schematic diagram of dip coating method and corresponding SEM image

1μm

- We have used sequential dip and drying methods to make all the coatings.

- After every dip, we give enough time for small nucleation and stop the process when desired particle size is achieved
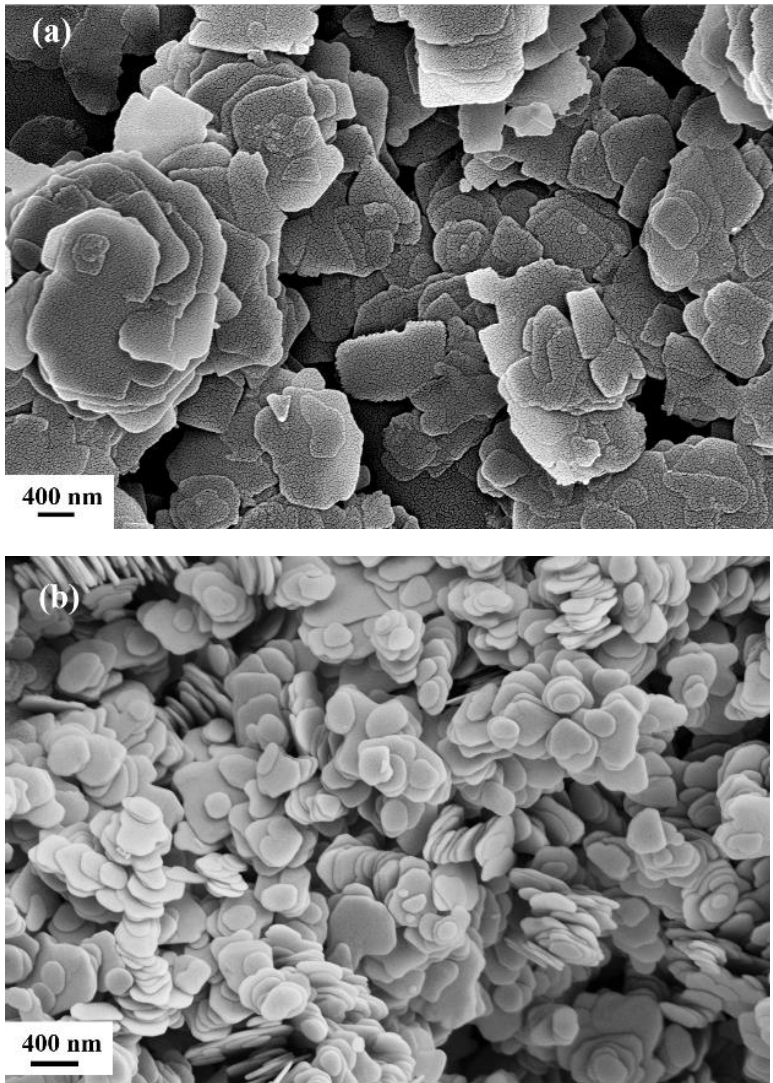
**Fig 11.** SEM image of MABiCl perovskite (a) powder sample (b) thin-film sample using the dip-coating method.

- The powder sample shows irregular and non-uniform growth.
- The thin-film sample shows the growth of distinct flakes with large surface coverage and uniformity.
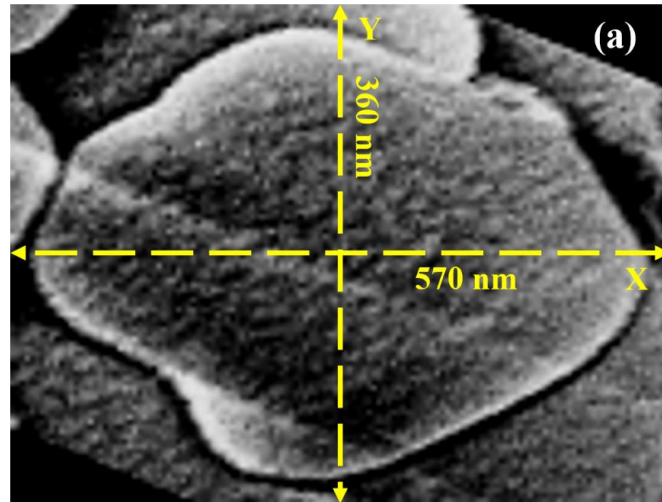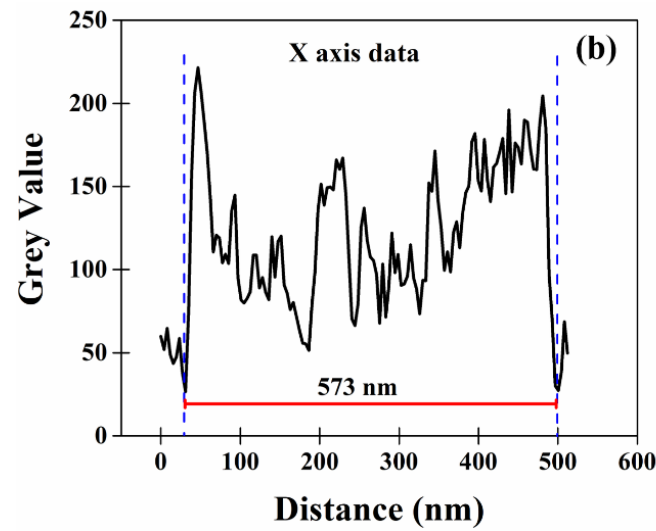
**Fig 12.** (a) Flat surface of a clear flake with length along the X-axis is 570 nm and along Y-axis of 360 nm,

(b) The plot of the grey value of the pixels and distance of the pixel from the initial along the X-axis for the flat surface

(c) The plot of the grey value of the pixels and distance of the pixel from the initial point along the Y-axis for the flat surface.
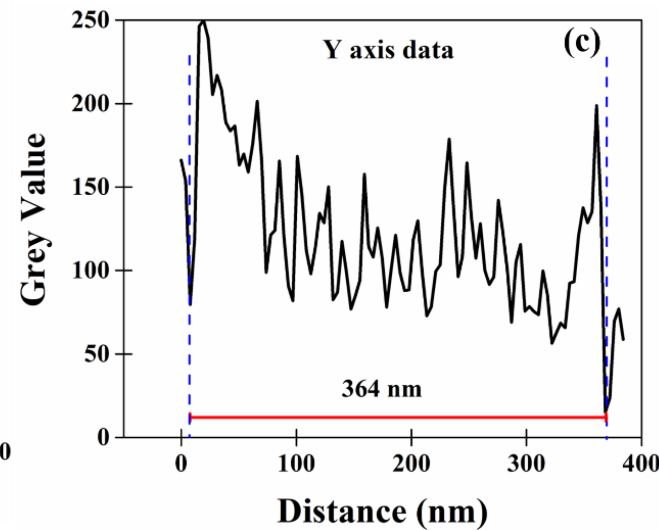
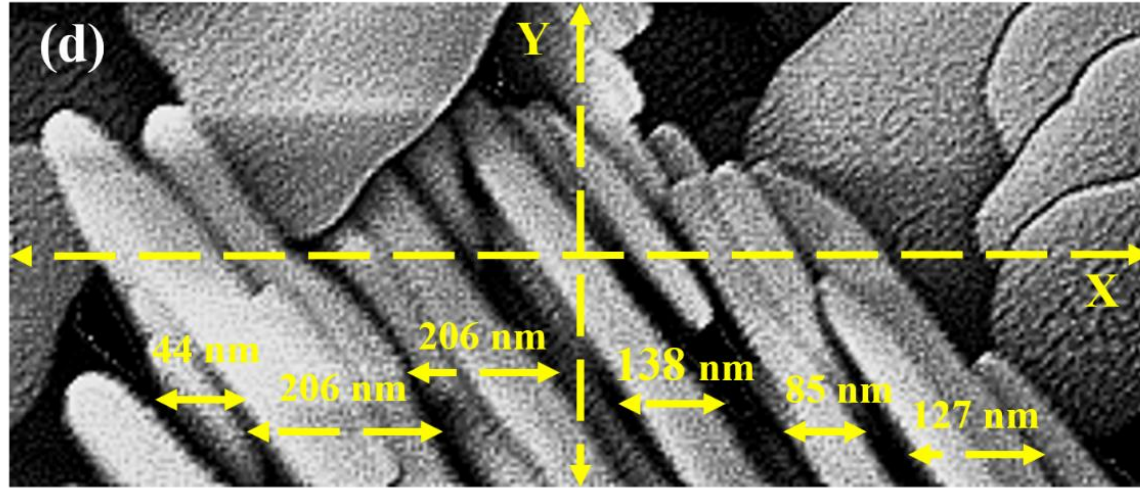Length of the flat surface of the flake along X direction is 570 nm, and along Y axis is 360 nm

**Fig 12.** (d) a cluster of flakes having visibly distinct flakes with thicknesses 44 nm, 206 nm, 206 nm, 138 nm, 85 nm, and 127 nm, respectively, from the left.

(e) the plot of the grey value of the pixels and distance of the pixel from initial along X axis for the perpendicular surfaces of the flakes and

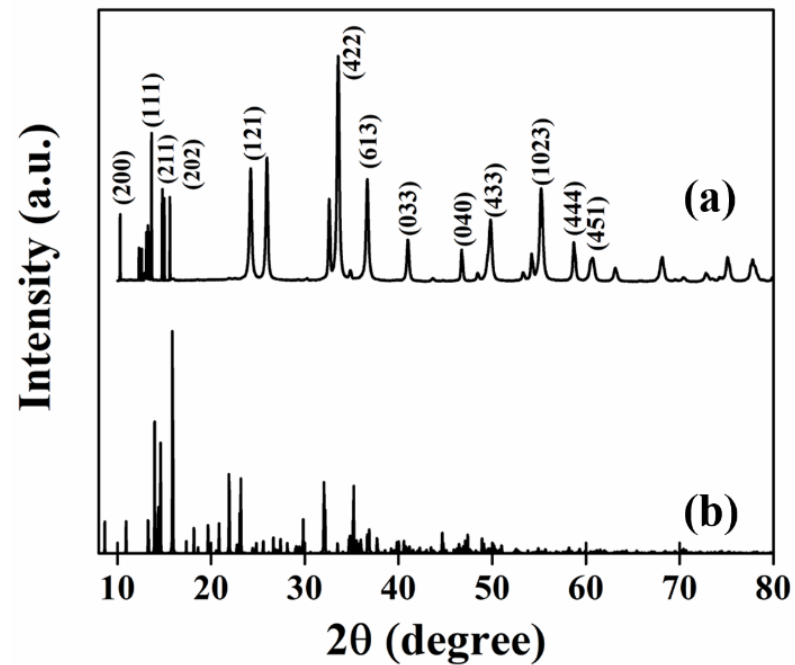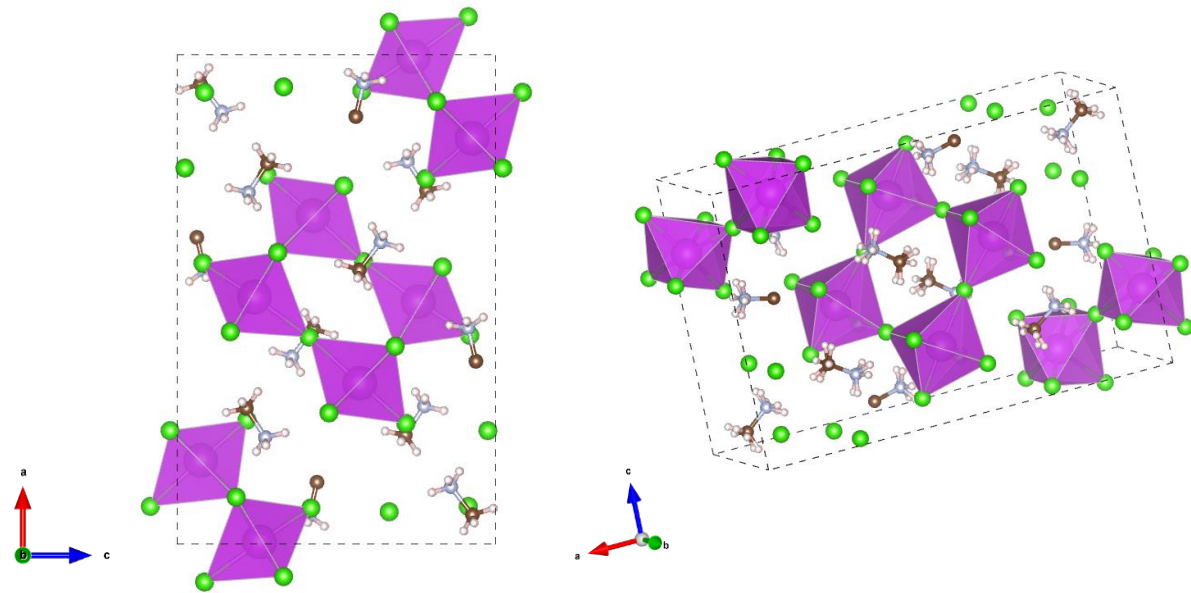(f) the thickness of each flake vs. flake index.
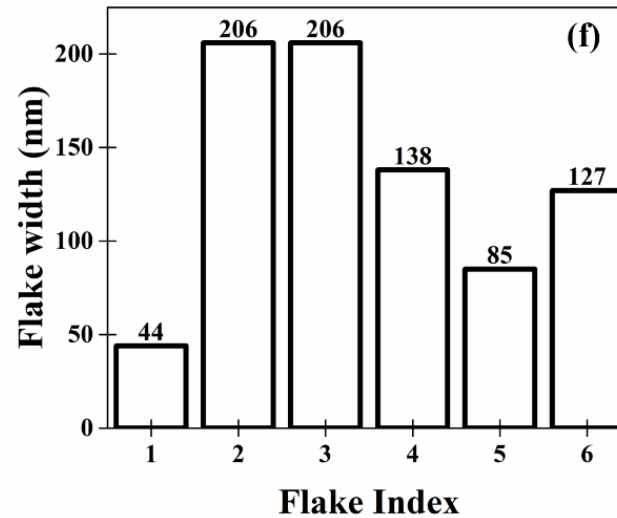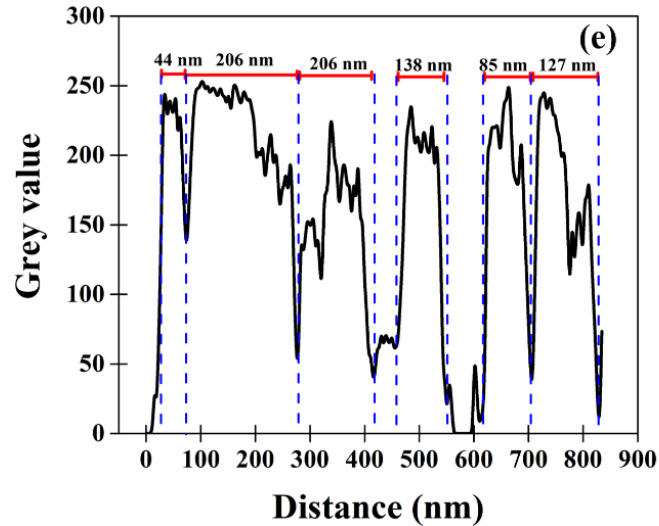
**Fig 13**: XRD pattern of (a) the synthesized MABiCl perovskite film and that of (b) provided by the Crystallographic Information File (CIF).



- XRD pattern showed a high degree of crystallinity

- The material's crystal structure belongs to the centrosymmetric orthorhombic Pnma space group.

- We have found some additional small peaks probably arising from the substrate and unreacted Bi.
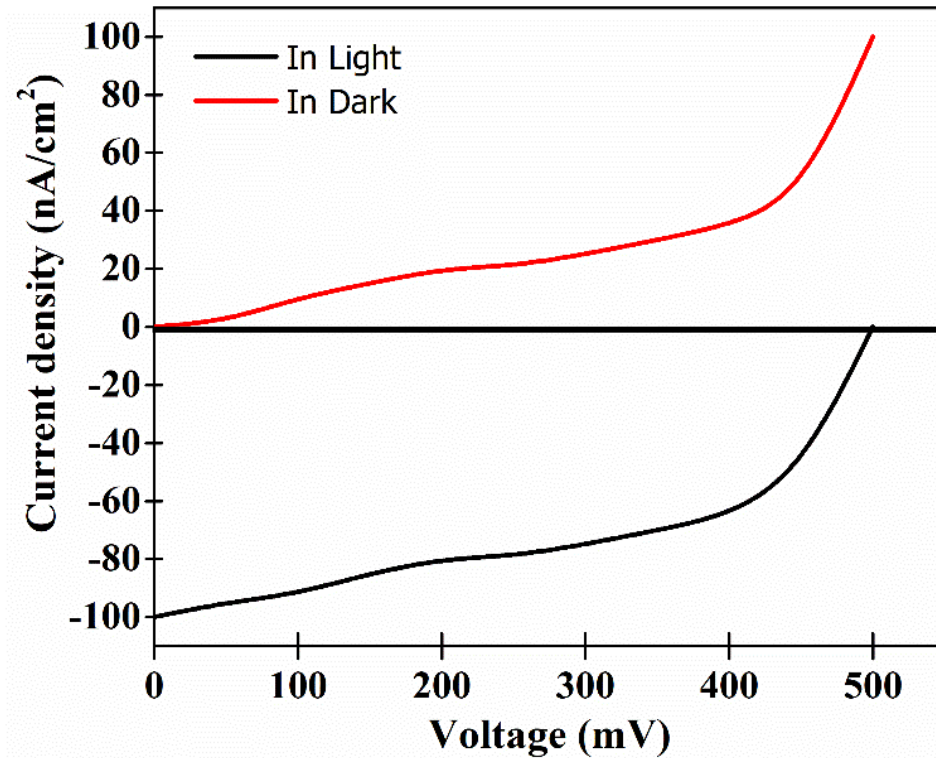
**Fig 14:** J-V characteristic curve of the ITO/Meso-TiO$_2$/ [(CH$_3$NH$_3$)$_3$Bi$_2$Cl$_9$]$_n$/Ag/ITO device.
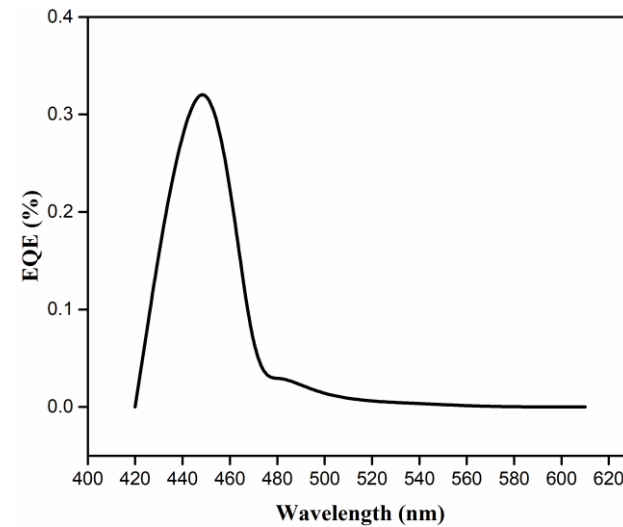


**Fig. 15:** External quantum efficiency of the solar cell device.

- Open circuit voltage (V$_{OC}$) = 496 mV

- Fill-factor (FF) = 0.55

- Short-circuit current density (J$_{SC}$) = 100 nA/cm$^2$

- Efficiency = ~ 0.1%

| Light absorber | $V_{OC}$ (mV) | Fill-actor (FF) | Published in year | Ref. |
|:---:|:---:|:---:|:---:|:---:|
| 1,6-hexanediammonium bismuth iodide (HDABiI$_5$) | 384 | 0.43 | 2016 | J. Mater. Chem. 4 (2016) 6837. |
| (CH$_3$NH$_3$)$_3$Bi$_2$I$_9$Cl$_X$ | 40 | 0.38 | 2015 | Adv. Mater. 27 (2015) 6806. |
| (CH$_3$NH$_3$)$_3$CuCl$_2$Br$_2$ | 300 | 0.32 | 2016 | Inorg. Chem. 55 (2016) 1044. |
| (CH$_3$NH$_3$)$_3$Bi$_2$I$_9$ | 680 | 0.33 | 2015 | Adv. Mater. 27 (2015) 6806. |
| (CH$_3$NH$_3$)$_3$Bi$_2$I$_9$ | 354 | 0.454 | 2016 | Nano Res 9 (2016) 692. |
| 1D polymer- [(CH$_3$NH$_3$)$_3$Bi$_2$Cl$_9$]$_n$ | 430 | - | 2018 | ACS Appl. Energy Mater. 1 (2018) 2405. |
| [(CH$_3$NH$_3$)$_3$Bi$_2$Cl$_9$]$_n$ | **496** | **0.55** | **2021** | **This work** |

# A dielectric study of Br-doped lead-free methylammonium bismuth chloride $(CH_3NH_3)_3Bi_2Br_xCl_{9-x}$
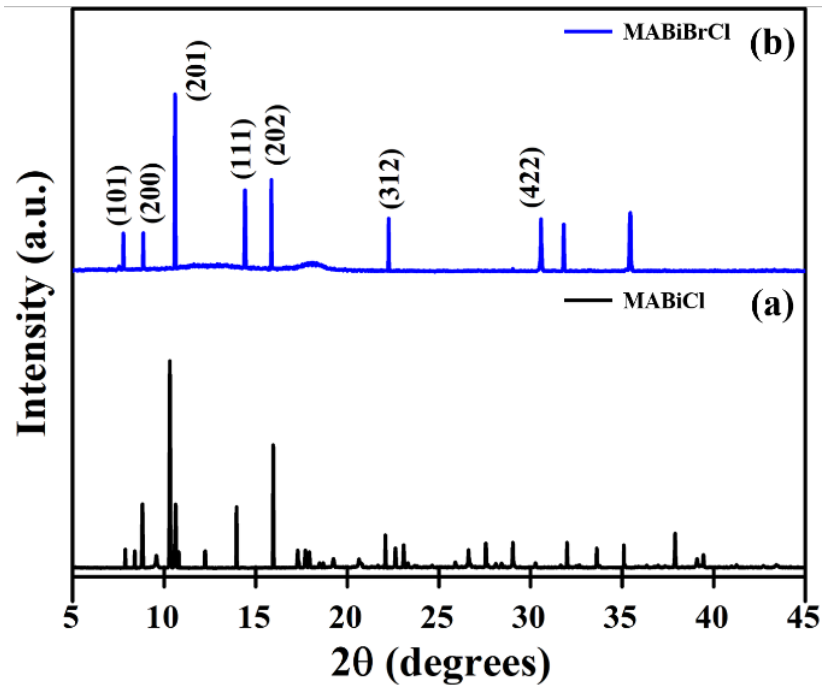
**Fig 16.** X-Ray diffraction (XRD) pattern for (a) $(CH_3NH_3)_3Bi_2Cl_9$ (MABiCl) and (b) $(CH_3NH_3)_3Bi_2Br_xCl_{9-x}$ (x = 3) (MABiBrCl).
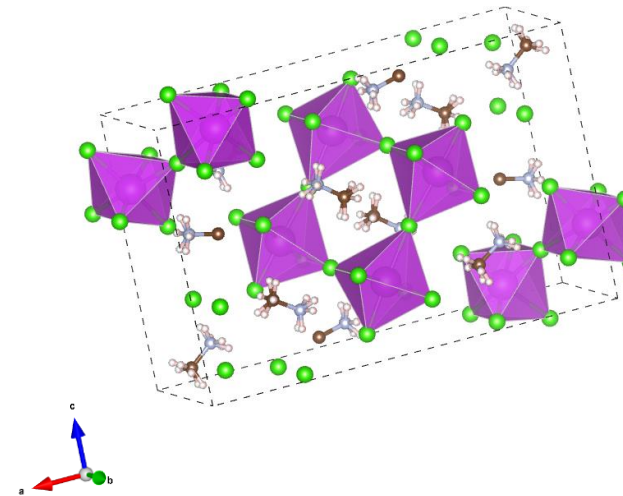


- The XRD pattern for both the samples depicts a monoclinic structure with P21/n symmetry.

- We observed a small shift in some peaks which may be attributed to the micro-strain developed due to difference in ionic radii of Br and Cl ions.
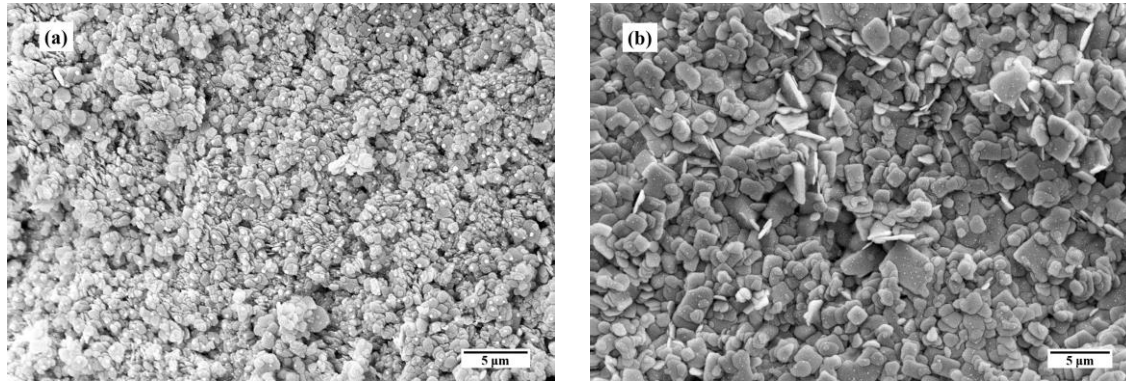
**Fig 17**. SEM image of (a) $(CH_3NH_3)_3Bi_2Cl_9$ (MABiCl) and (b) $(CH_3NH_3)_3Bi_2Br_xCl_{9-x}$ (x = 3) (MABiBrCl).
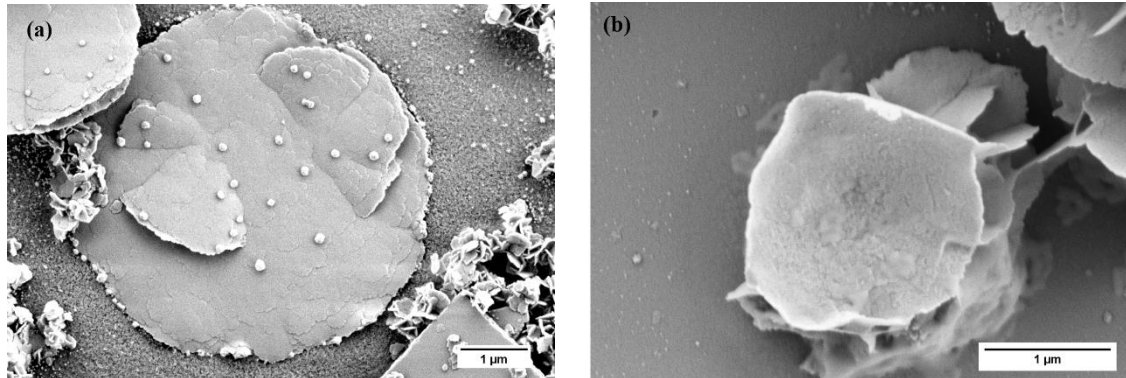


**Fig 17.** Large scale view of SEM morphology of the pelletized sample of (a) MABiCl and (b) MABiBrCl.

- We observed that the microstructure contains disc-like flakes ranging from 100 nm to 5 μm.

- Br doping tends to produce a bending on the edge of the disc-like shapes.

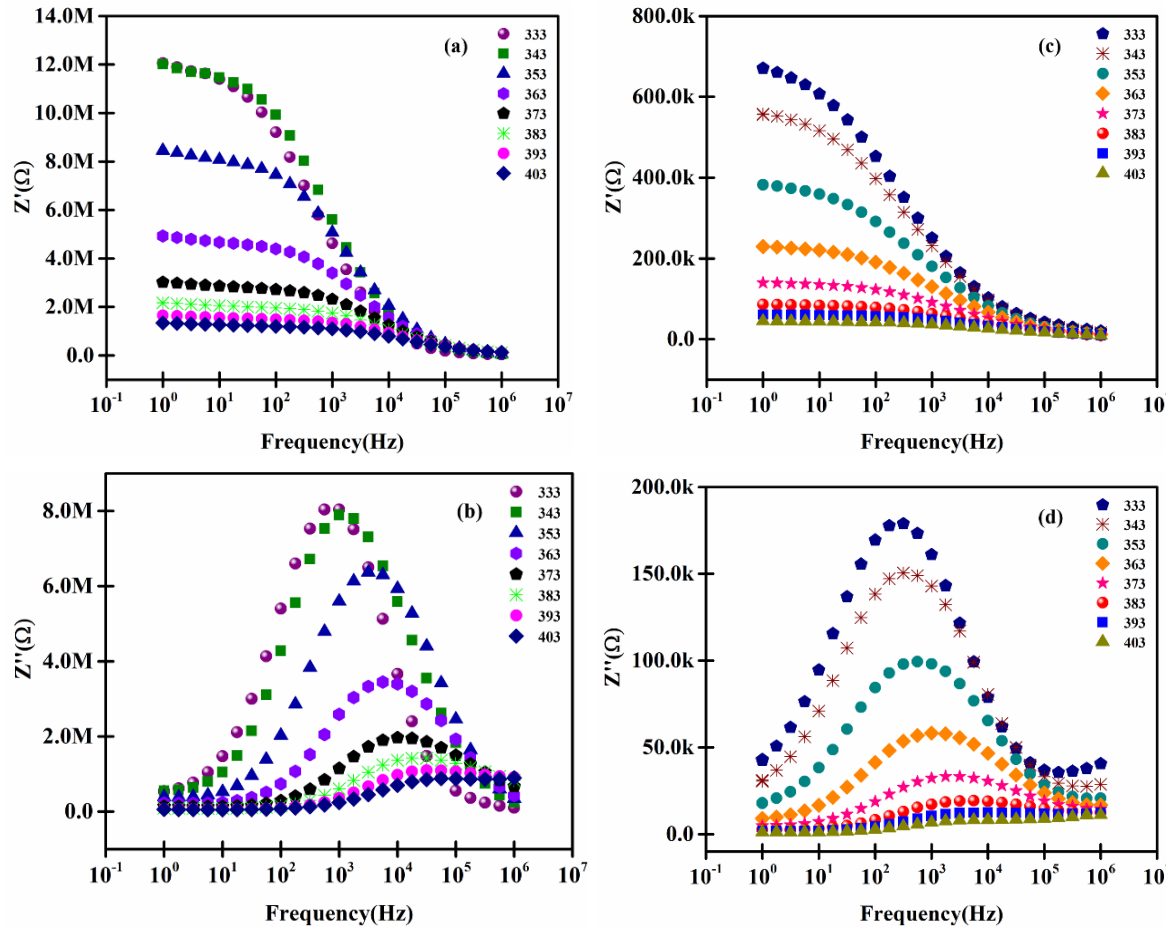- Br doped sample shows a visible increase (~ 100-300 nm) in grain size.

**Fig 18.** Impedance spectroscopy in the range 333K–403K. (a), (b), (c), (d) Real and imaginary part of impedance vs. frequency for sample MABiCl and MABiBrCl.

- $Z'$ decreases with the increase in frequency as well as temperature and indicates the negative temperature coefficient of resistance (NTCR)-type behaviour.

- The $Z''$ data shows a distinct peak corresponding to a relaxation frequency and the peak is found to be shifted to higher frequency with increasing temperature indicating thermal dependence of the relaxation process.

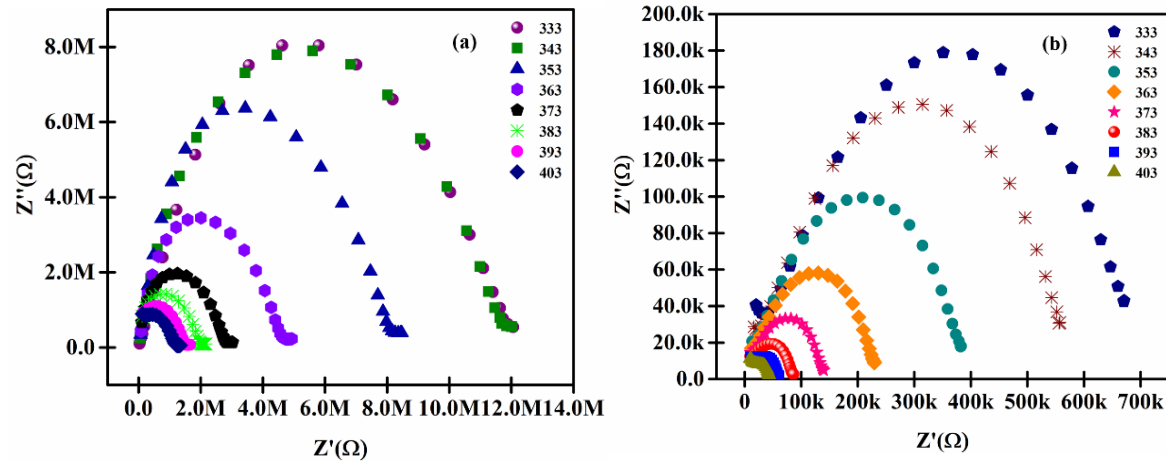- Furthermore, reduction of the peak height with temperature is also observed.

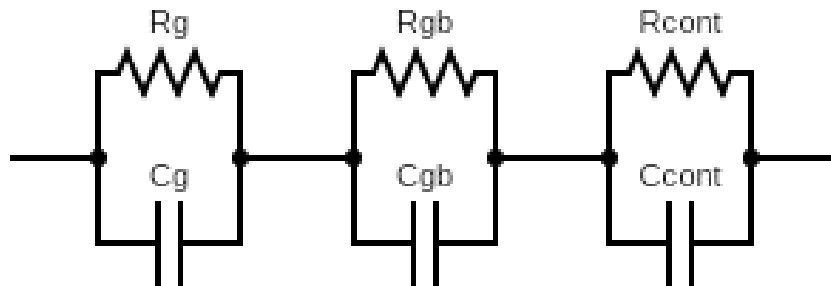Fig. Cole–Cole plot for (a) MABiCl sample and (b) MABiBrCl sample.



**Fig 19.** Equivalent circuit diagram.

- The Cole-Cole plot shows semicircular arcs and is modelled by an equivalent circuit consisting of parallel RC combinations as shown in Figure below.

- We observed that the radii of the semicircles decrease with increasing temperature which confirms again the NTCR behavior of both the materials.
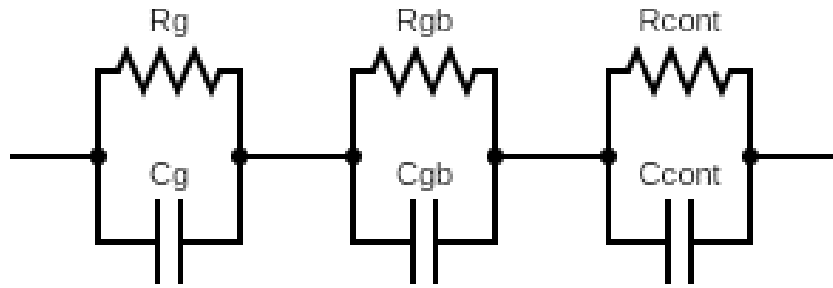
Grain contribution

Grain boundary contribution

Contact contribution

**Fig 20.** Schematic diagram of the transport process
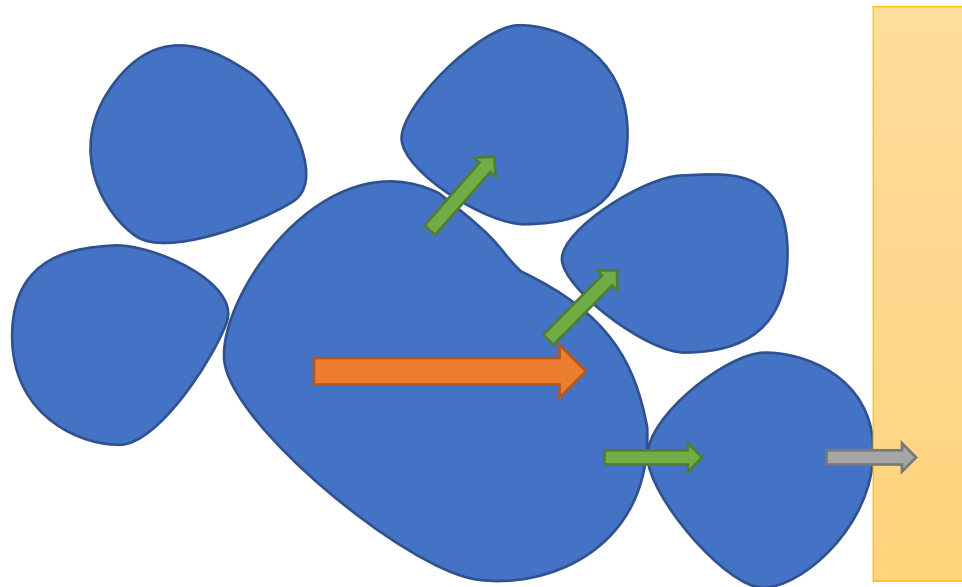
$$Z'(\omega) = \frac{R_g}{\left[1 + \left(\omega R_g C_g\right)^2\right]} + \frac{R_{gb}}{\left[1 + \left(\omega R_{gb} C_{gb}\right)^2\right]} + \frac{R_c}{\left[1 + (\omega R_c C_c)^2\right]}$$

$$Z''(\omega) = \frac{C_g R_g}{\left[1 + \left(\omega R_g C_g\right)^2\right]} + \frac{\omega C_{gb} R_{gb}}{\left[1 + \left(\omega R_{gb} C_{gb}\right)^2\right]} + \frac{\omega C_c R_c}{\left[1 + (\omega R_c C_c)^2\right]}$$

**Fig 21.** The plot of the variation of (a) $R_{cont}$, $R_{gb}$, $R_g$ and (b) that of $C_{cont}$, $C_{gb}$, $C_g$ with temperature for sample MABiCl.
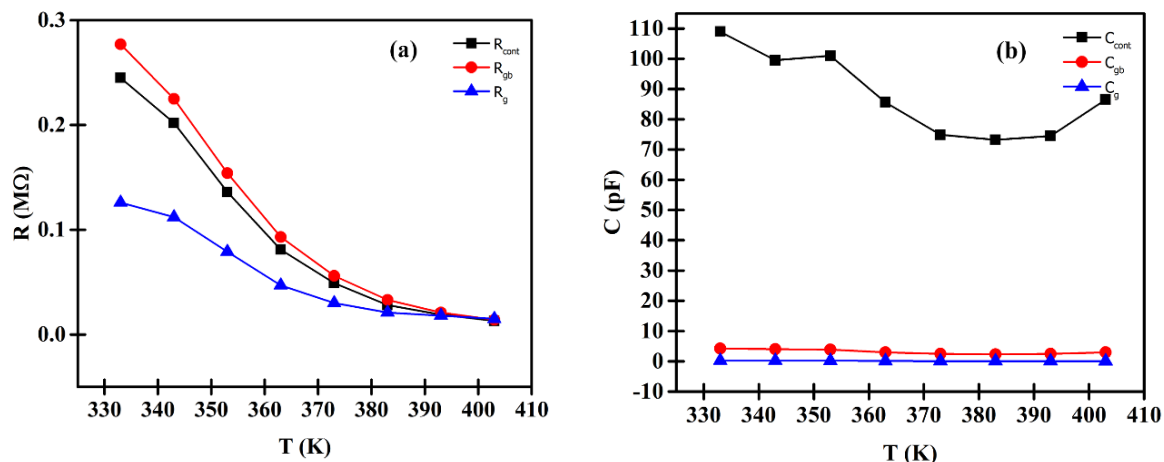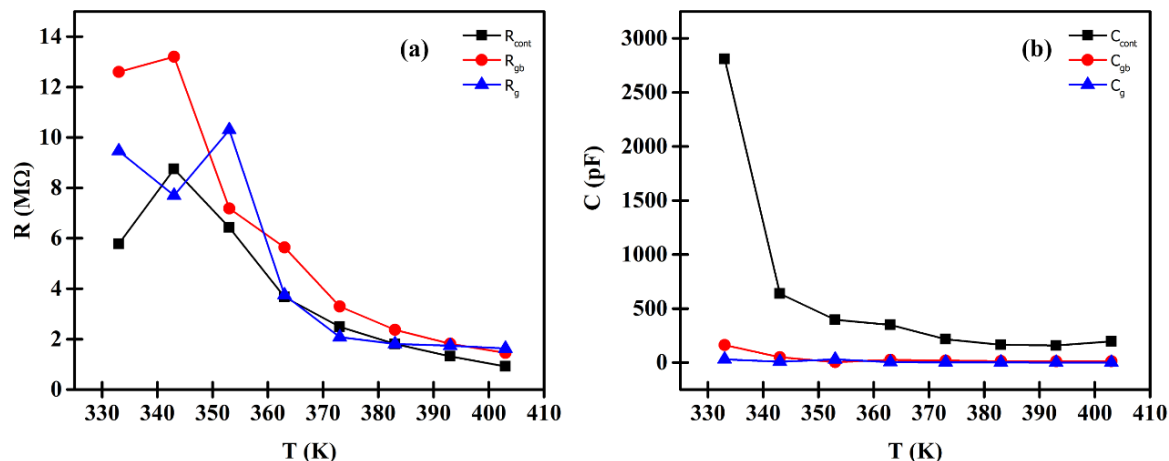


**Figure 22.** The plot of the variation of (a) $R_{cont}$, $R_{gb}$, $R_g$ and (b) that of $C_{cont}$, $C_{gb}$, $C_g$ with temperature for sample MABiBrCl.

- These three semicircles are primarily due to the contributions of electrode–material interface, grain, and grain boundary.
- Semicircle in the high-frequency region is attributed to the contribution of grains
- The low-frequency region is assigned to the contribution from the grain boundaries and the electrode–material interface.
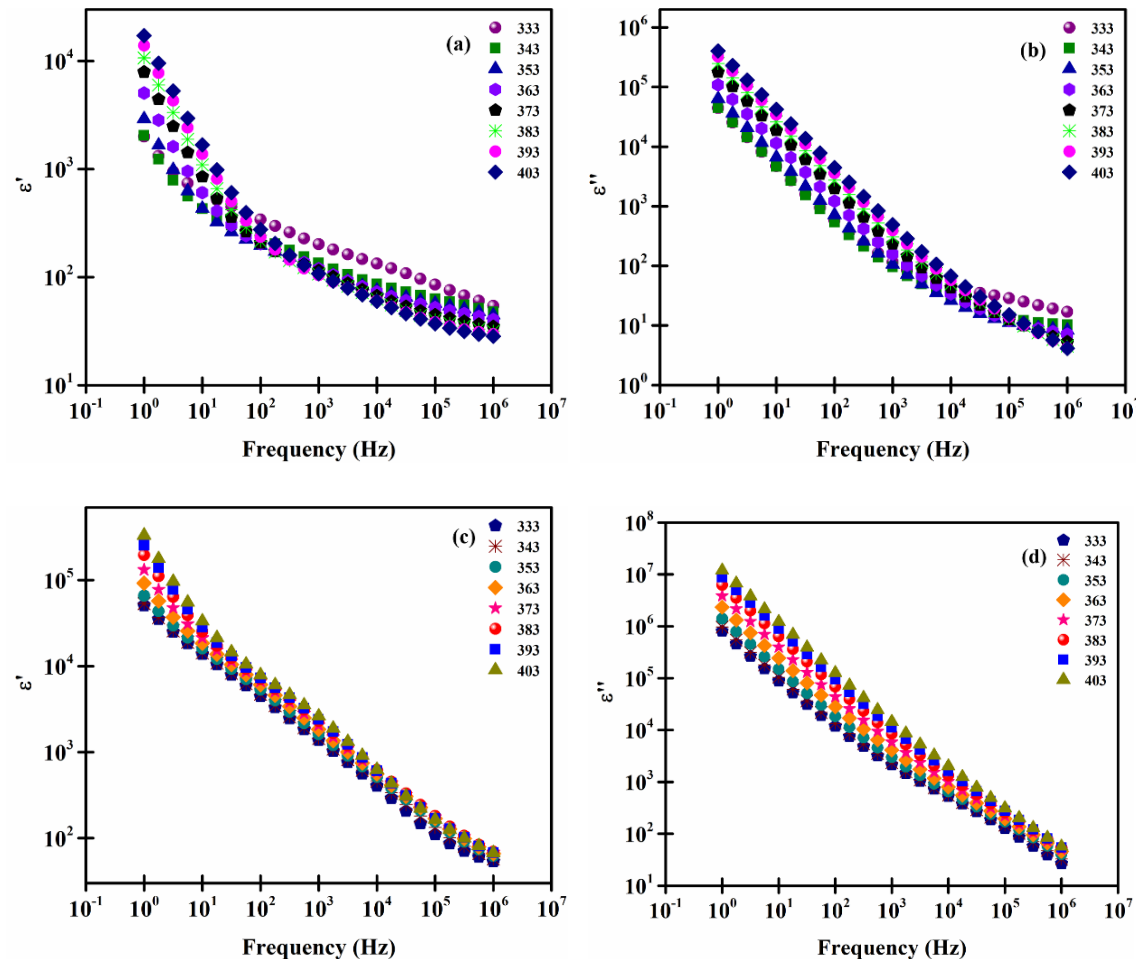
**Fig 23.** The frequency-dependent plot of the real and imaginary parts of $\varepsilon(\omega)$ of MABiCl and MABiBrCl.

- Semiconductors consist of frequency-independent DC conductivity which complicates any relaxation process
- Using Koop's theory the material is considered to be an inhomogeneous medium consisting of grains separated by definite boundaries with negligible conduction or high potential barriers.
- Under the influence of an applied alternating electric field, the electrons move toward the grain boundary by the hopping mechanism.
- Now, if the resistance is massive enough at the grain boundary, then the electrons may accumulate at the grain boundaries and produce polarization. But as the frequency increases the electron hardly copes up with rapid force field direction alteration which in turn reverses the electron flow and decrease in polarization.
- The ionic polarization within the material arises due to the separation of negative $((Bi_2X_9)^{3-})$ and positive $MA^+$ charge centres. Higher values of $\varepsilon'(\omega)$ at low frequencies may be attributed to the contribution of ionic polarization within the material.
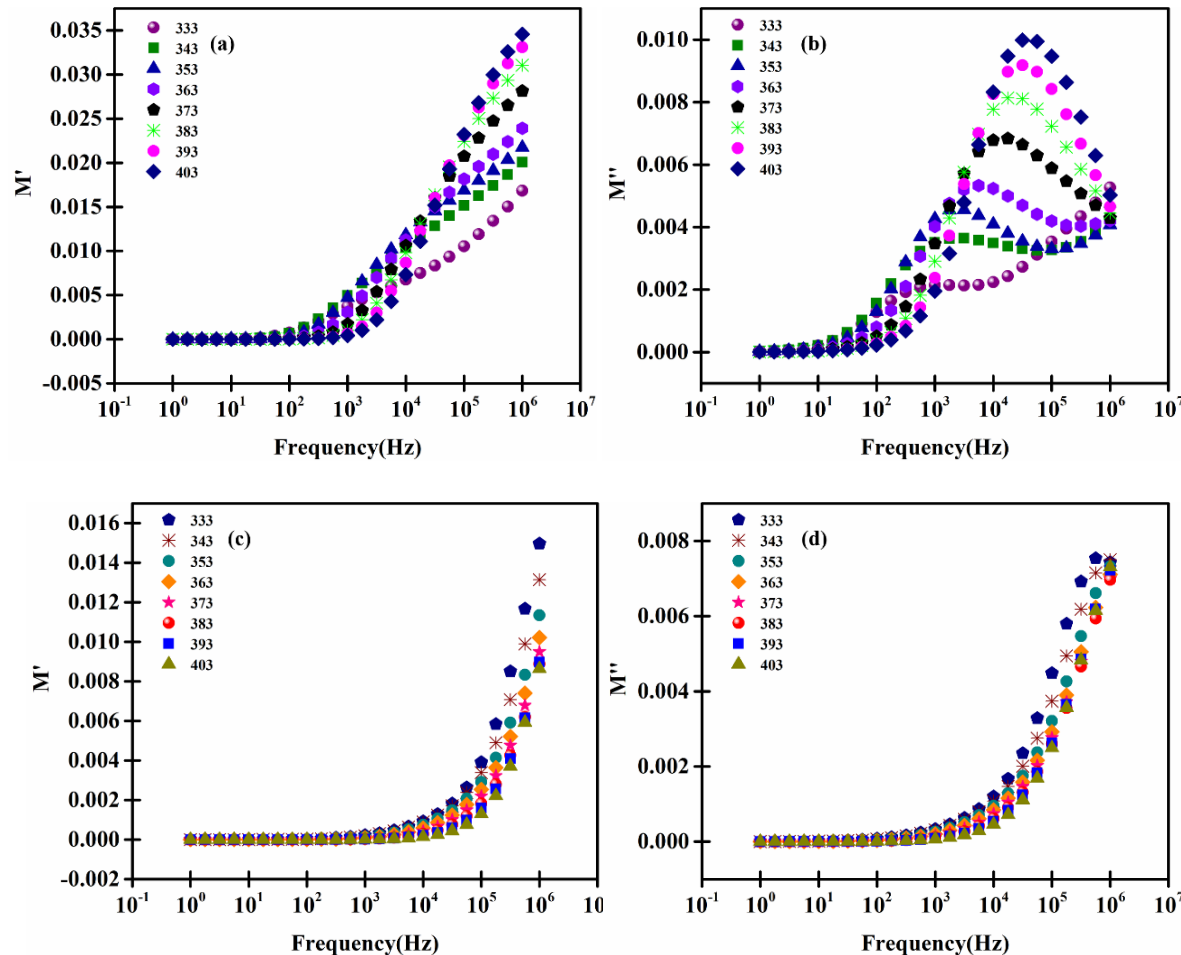
**Fig 24.** Logarithmic angular frequency dependence of $M'$ and $M''$ (a, b) of MABiCl and (c, d) of MABiBrCl.

- The relaxation phenomenon inside both materials gives rise to a characteristic peak ($f_{max}$) which tends to shift toward higher frequencies with the increase in temperature which can be caused by the movement of free charges generated by thermal energy.
- The frequency variation of $M''(\omega)$ below $f_{max}$ is correlated to the hopping of mobile charge carriers over a long range inside the MABiCl and MABiBrCl and above $f_{max}$ to the short-range or localized motion of charge carriers.
- The relaxation peak points to the transition from the long-range to the short-range mobilization of free charges in MABiCl and MABiBrCl.
- The MABiBrCl sample shows the long-range electron hopping for a greater range of frequency values and the range increases with increasing temperature.
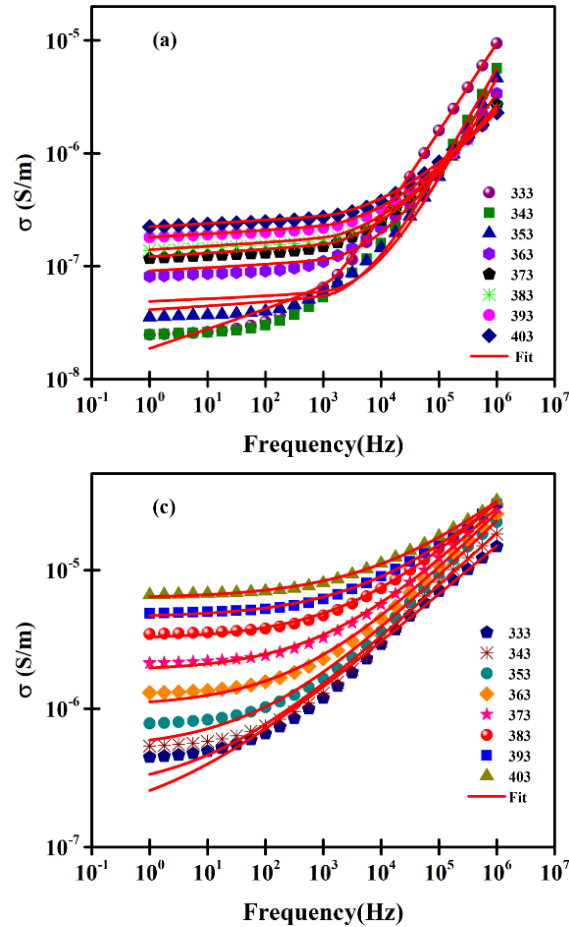
**Fig 25.** (a), (c) Electrical conductivity vs. frequency plot for temperature range 333-403K for MABiCl and MABiBrCl.

# Jonscher's power law

$$\sigma(\omega) = \sigma_{dc} + A\omega^n$$

- At low frequencies, the electrical conductivity is nearly equal to the dc conductivity, which does not change significantly up to a critical frequency and arises out of long-range hopping of charge carriers due to resistive grain boundaries.
- Beyond the critical frequency, as the frequency is increased, the conductivity increases nonlinearly. This is ascribed to the short-range hopping of charge carriers dominated by trap-controlled ac electrical conduction process.
- This is often described by a jump relaxation model (JRM model) to account for the dispersive nature of the conductivity at high frequency.
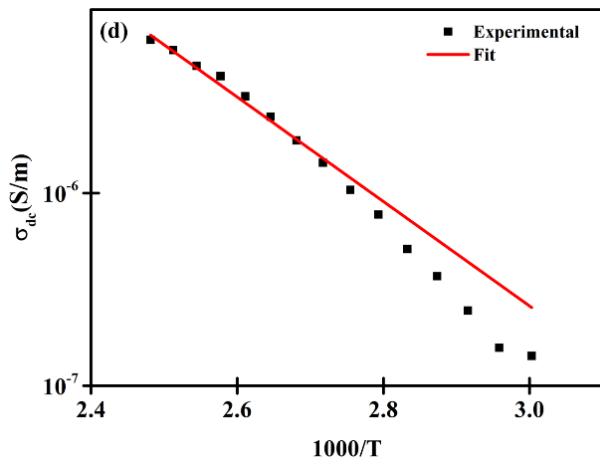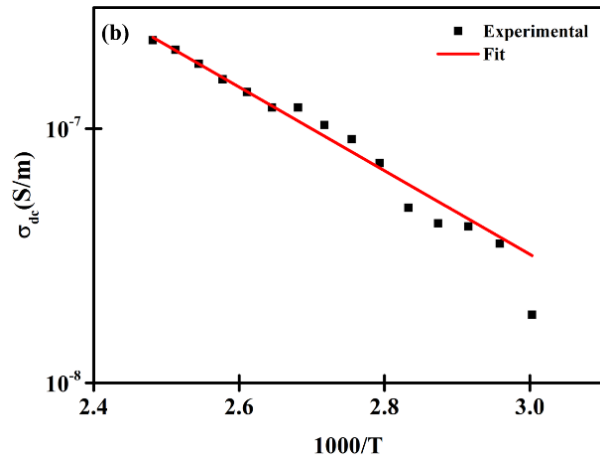
**Arrhenius relation**

$$\sigma_{dc} = \sigma_0 \exp\left(-\frac{E_a}{KT}\right)$$

- The activation energies are obtained from the Arrhenius plot as shown in Fig.
- Activation eneries are **0.326 eV** and **0.538 eV** for MABiCl and MABiBrCl respectively.

**Fig 26**. (b) Arrhenius plot of MABiCl. (d) Arrhenius plot of MABiBrCl.

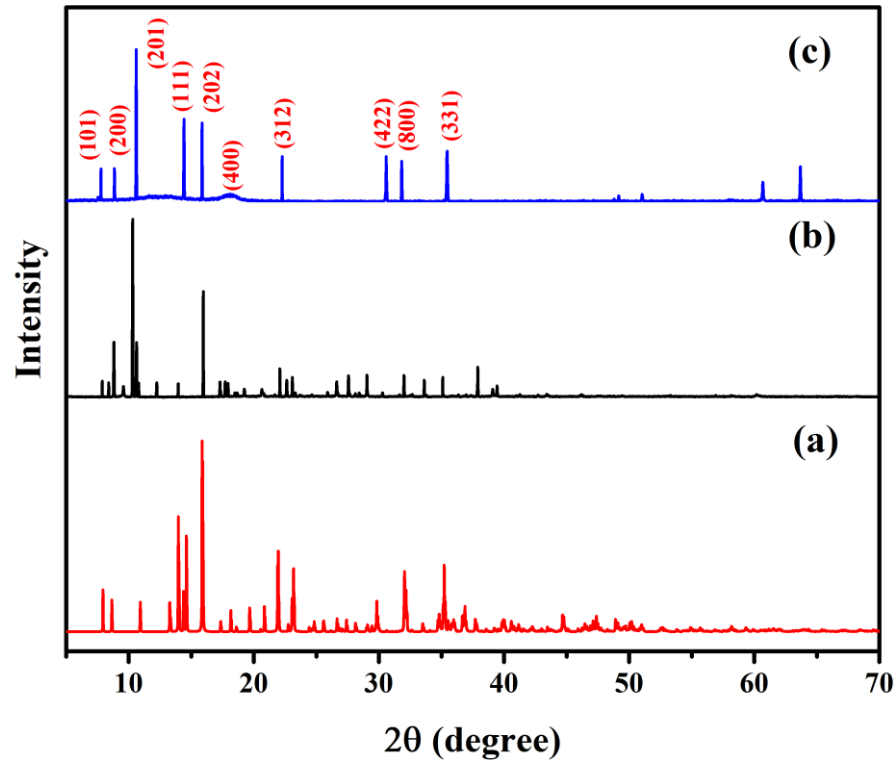# Frequency and temperature-dependent dielectric characteristics of lead-free Br doped perovskites $(CH_3NH_3)_3Bi_2Cl_9$ and $(CH_3NH_3)_3Bi_2Br_xCl_{9-x}$

**Fig 27.** X-Ray diffraction plot for (a) calculated from the CIF (a) $(CH_3NH_3)_3Bi_2Cl_9$ (MABiCl) and (b) $(CH_3NH_3)_3Bi_2Br_xCl_{9-x}$ (x = 3) (MABiBrCl).

| Angle (2θ) | Crystal indices (hkl) |
|---|---|
| 7.89° | (101) |
| 8.82° | (200) |
| 10.59° | (201) |
| 13.96° | (111) |
| 15.96° | (202) |
| 17.30° | (400) |
| 22.08° | (312) |
| 31.97° | (422) |
| 35.10° | (800) |
| 37.99° | (331) |

- For the doped samples, two additional peaks at 60.63° and 63.52° are obtained. The additional peaks observed may arise due to unreacted bismuth phase in the sample.
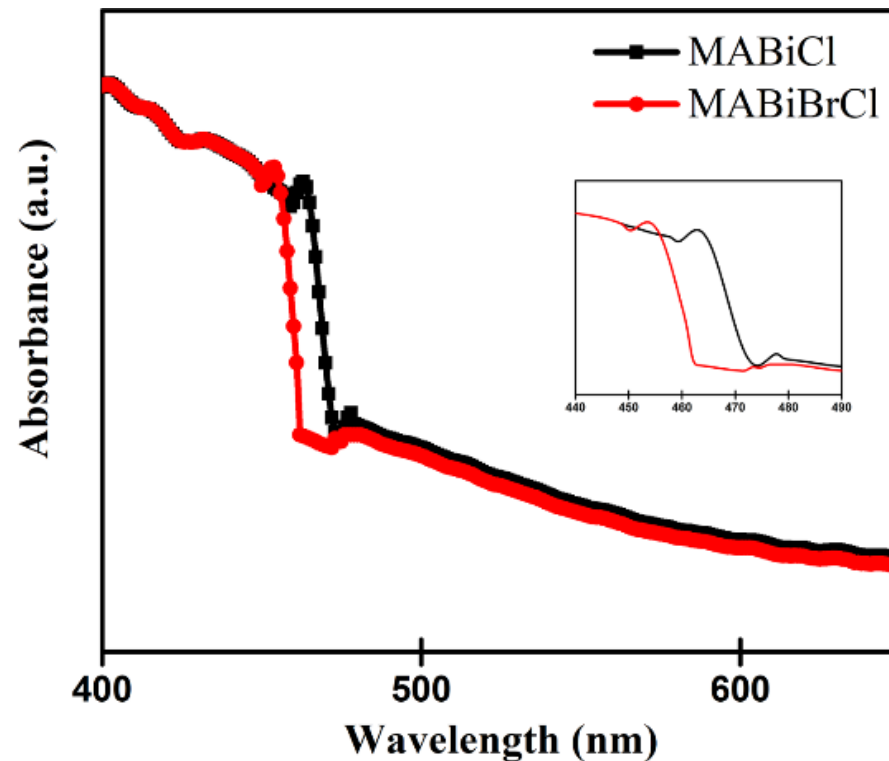
**Fig 28.** Optical absorption data for MABiCl and MABiBrCl samples

- The bandgaps are calculated from the optical absorption data are **2.65** and **2.70 eV** for MABiCl and MABiBrCl respectively.
- Slight increase (50 meV) in bandgap is observed for the Br doped sample.
- Conventionally, the band gap decreases in perovskites when the ionic radius of the halogen ion increases but we observed a slight discrepancy in our result where bandgap increases with Br doping.
- This anomaly may be explained due to size effect of the perovskites flakes. Dependence of optical absorbance with the particle size of the sample is an observed phenomenon.
- Introduction of Br during synthesis plausibly resulted in a reduction of particle (flake) size (as seen in FESEM images) and hence the blue-shift of absorption peak and increase in band gap energy.
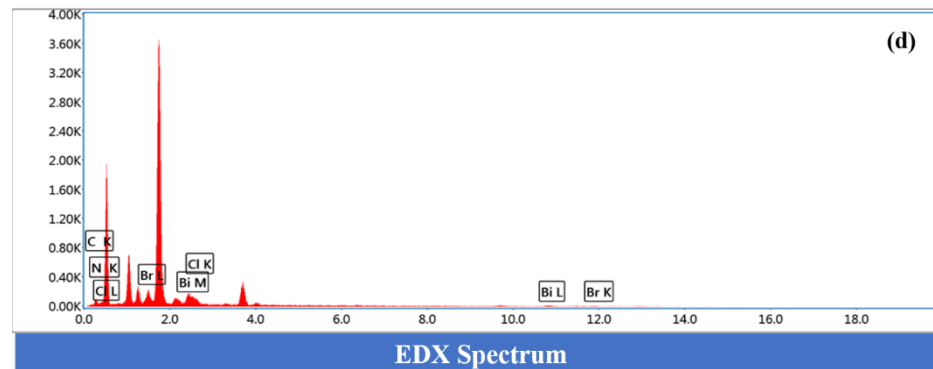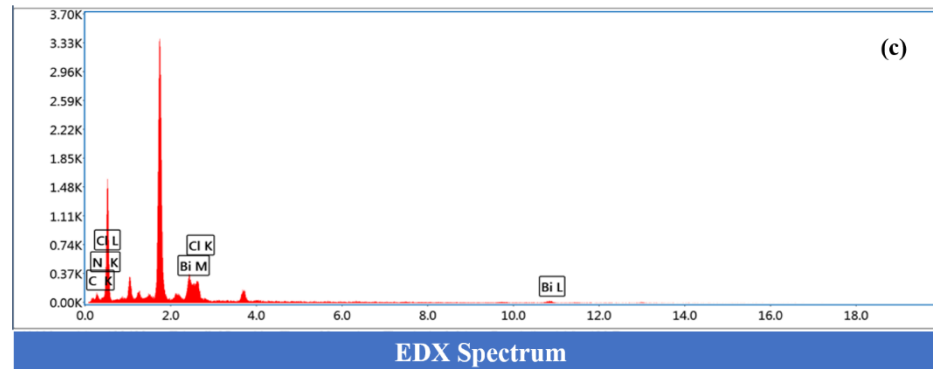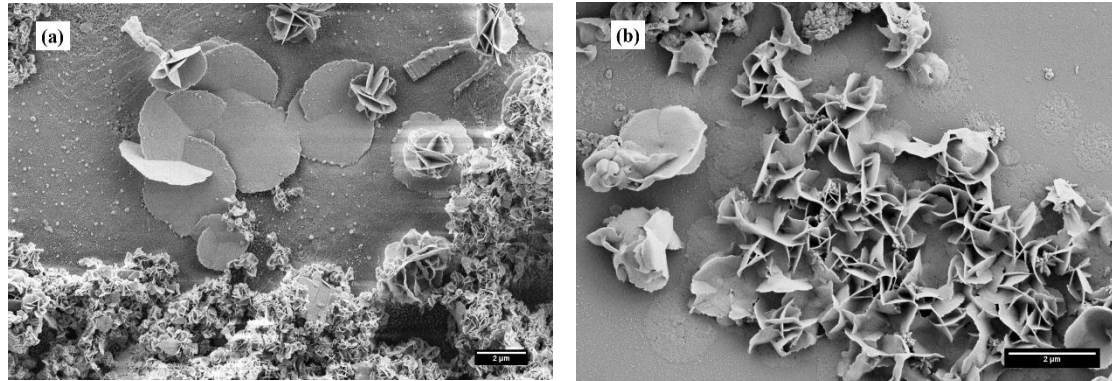
- The morphological structure of MABiCl and MABiBrCl samples is shown
- It is observed that the microstructure contains disc-like flakes ranging from 100 nm to 5 μm.
- The EDX spectra of the samples as shown confirm the presence of constituent elements (C, N, Cl, Br, Bi).
- The distribution of flakes was more uniform for Br doped than the MABiCl sample.

**Fig 29.** SEM image of (a) $(CH_3NH_3)_3Bi_2Cl_9$ (MABiCl) and (b) $(CH_3NH_3)_3Bi_2Br_xCl_{9-x}$ (x = 3) (MABiBrCl). The SEM showed growth of disc-shaped flakes for both the samples. EDX spectra are shown in (c) MABiCl and (d) MABiBrCl respectively.
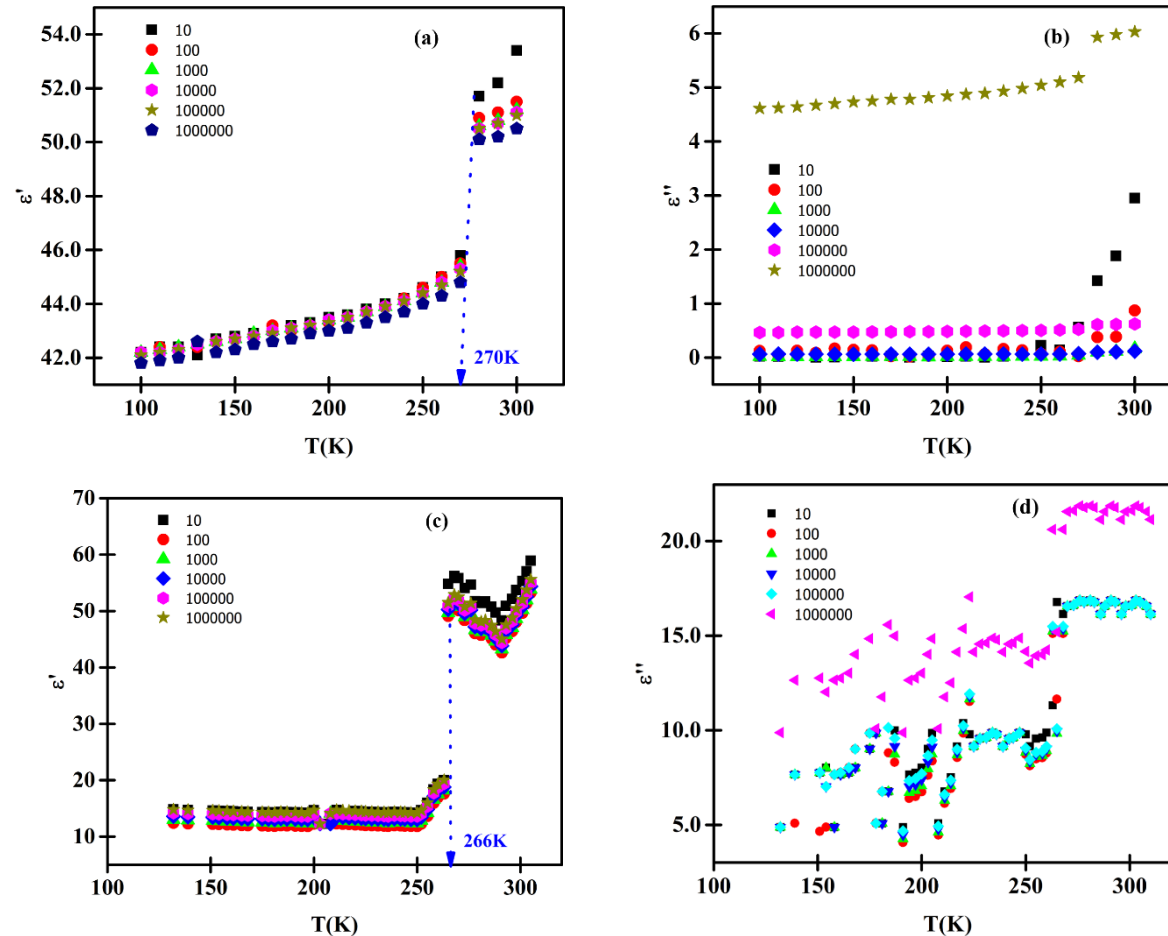
**Fig 30.** The temperature-dependent plot of dielectric permittivity's real and imaginary parts at different frequencies. (a) real part $\varepsilon'(\omega)$ and (b) imaginary part $\varepsilon''(\omega)$ MABiCl sample. (c) real part $\varepsilon'(\omega)$ and (d) imaginary part $\varepsilon''(\omega)$ for MABiBrCl.

- We have observed a sudden leap of $\varepsilon'$ at temperature $\sim$ 270K and $\sim$ 266 K for MABiCl and MABiBrCl, respectively. This plausibly results from a structural phase transition as reported by Belkyal *et al*. from XRD data.
- The MA ion present inside the structure is disordered in orientations relative to the rotation around the C-N axis. The permittivity value is almost constant below a specific temperature.
- When a critical temperature is reached, the MA ions achieve a new rotational degree of freedom and change the intrinsic crystal structure of the samples. We find that the critical temperature of transition is lower for Br doped sample. So, doping may be a viable option to tweak the transition temperature for any practical purpose.

# Observation of negative photoconductivity in $(CH_3NH_3)_3Bi_2(Br_xCl_{1-x})_9$: correlating ion-migration, instability and efficiency in halide perovskite solar cell

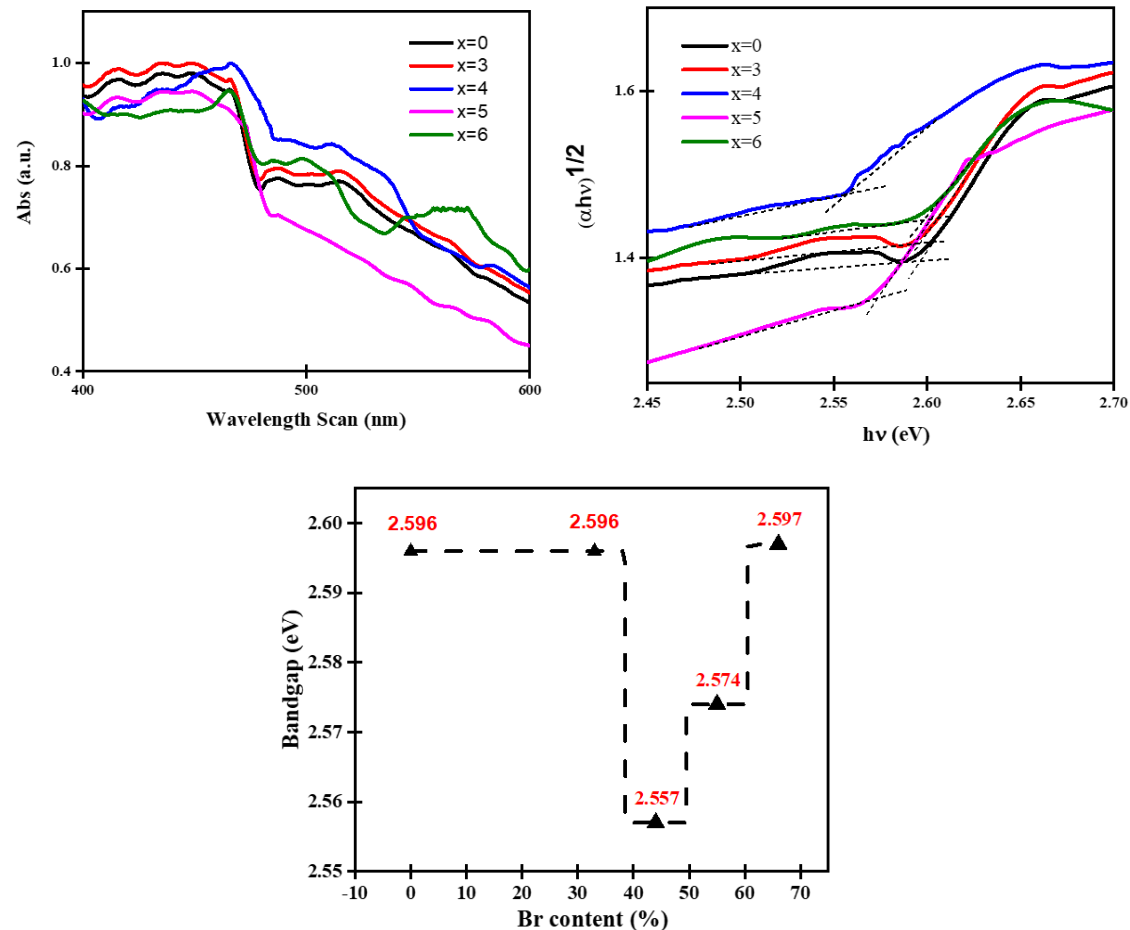**Fig 31.** (a) Absorption spectra, (b) corresponding Tauc plot for the samples $MABiBr_xCl_{(1-x)}$ where x = 0, 0.33, 0.0.44, 0.55, 0.66. (c) Comparison of bandgap with Br content.

- The band gaps for x=0.44 and 0.55 are found to drop significantly from their pristine value (2.596 eV) and then increase again to their pristine value for x=0.55.

- The bandgap exhibits a minimum value of 2.557 eV for Br content x=0.44, indicating plausibly a particular phase of perovskite structure with the lowest bandgap.

- It can be postulated that there are stable states in all this configuration, i.e., x = 0.44 where the band gap is minimum. For x = 0, there is no chance of change in the bandgap, so it shows a band gap of 2.596 eV.

- For dopped samples, when x = 0.44, a new stable phase is possible.
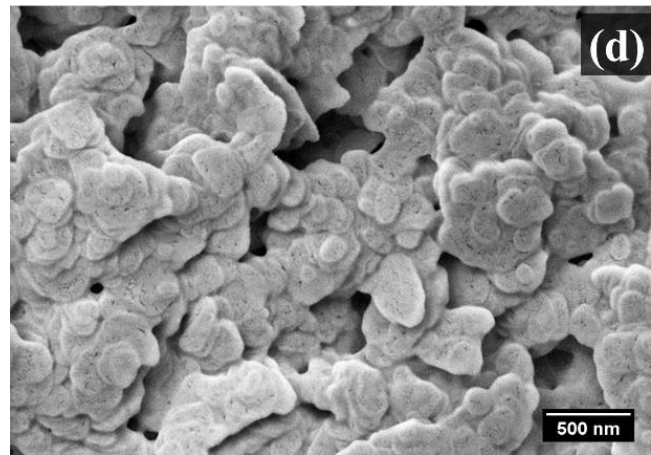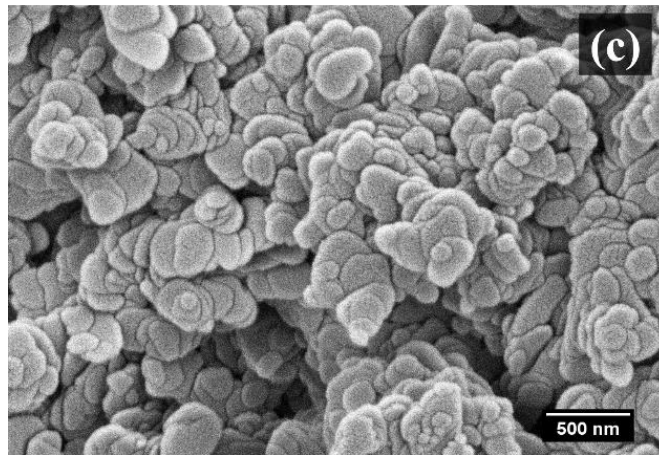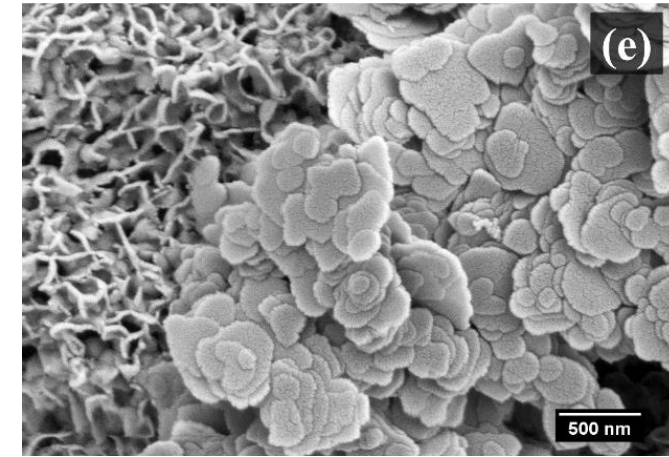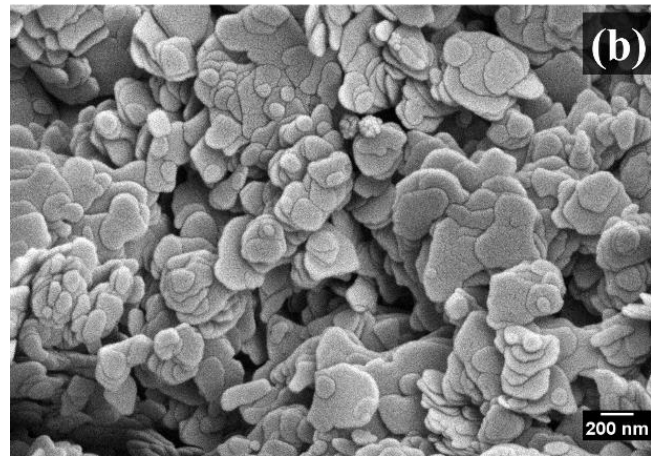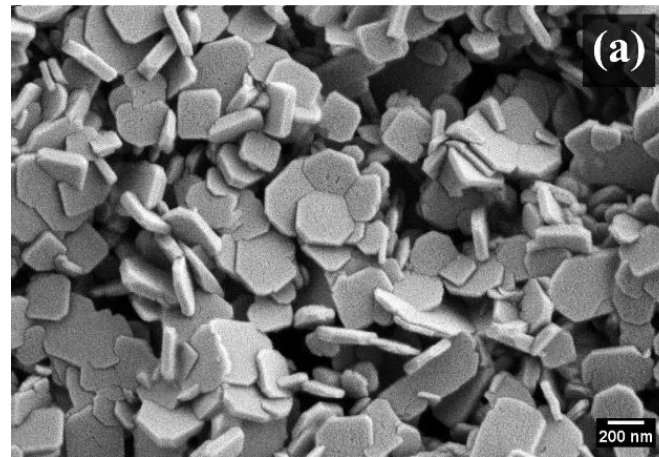
- In our previous works, we observed the flake curving effect with increased Br concentration.
- The grain size distribution is 200-300 nm which is small.
- Coexistence of flat and curved flakes is observed.

**Fig 32.** (a), (b), (c), (d), (e) shows the SEM images for samples with x = 0, 0.33, 0.0.44, 0.55, and 0.66, respectively. (f) depicts the EDX spectrum for all samples.
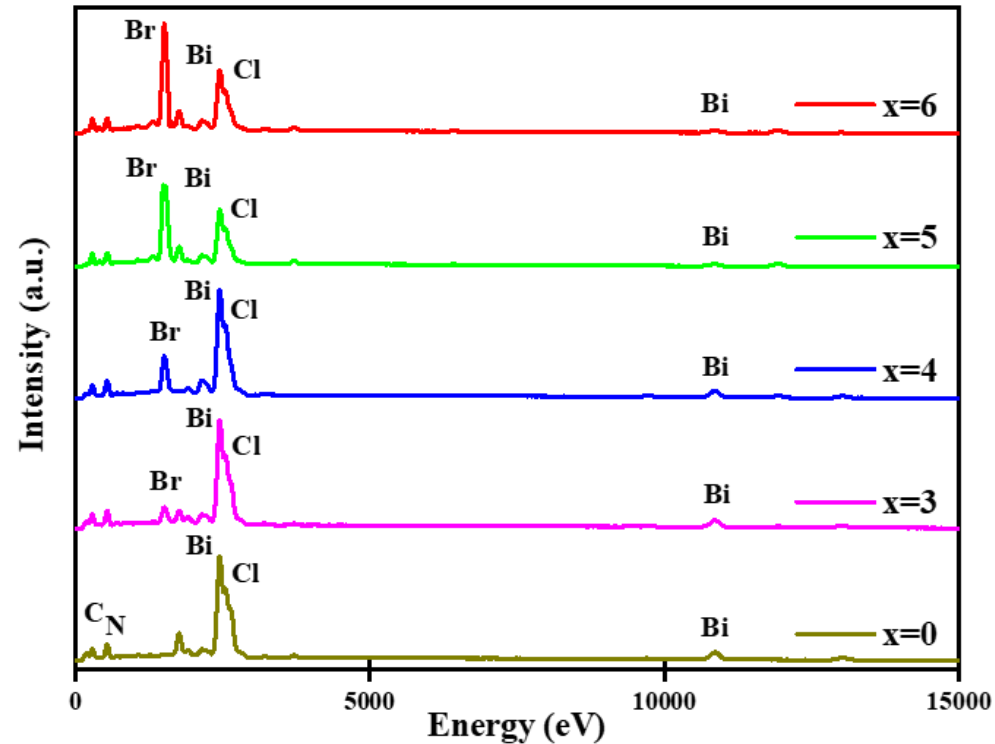
**Fig 33.** Depicts the EDX spectrum for all samples.

- We can see that the Br percentage is increased, and the Cl percentage is decreased with an increase in Br doping amount.
- Bi percentage almost stays the same, directly signifying the formation of desired samples.
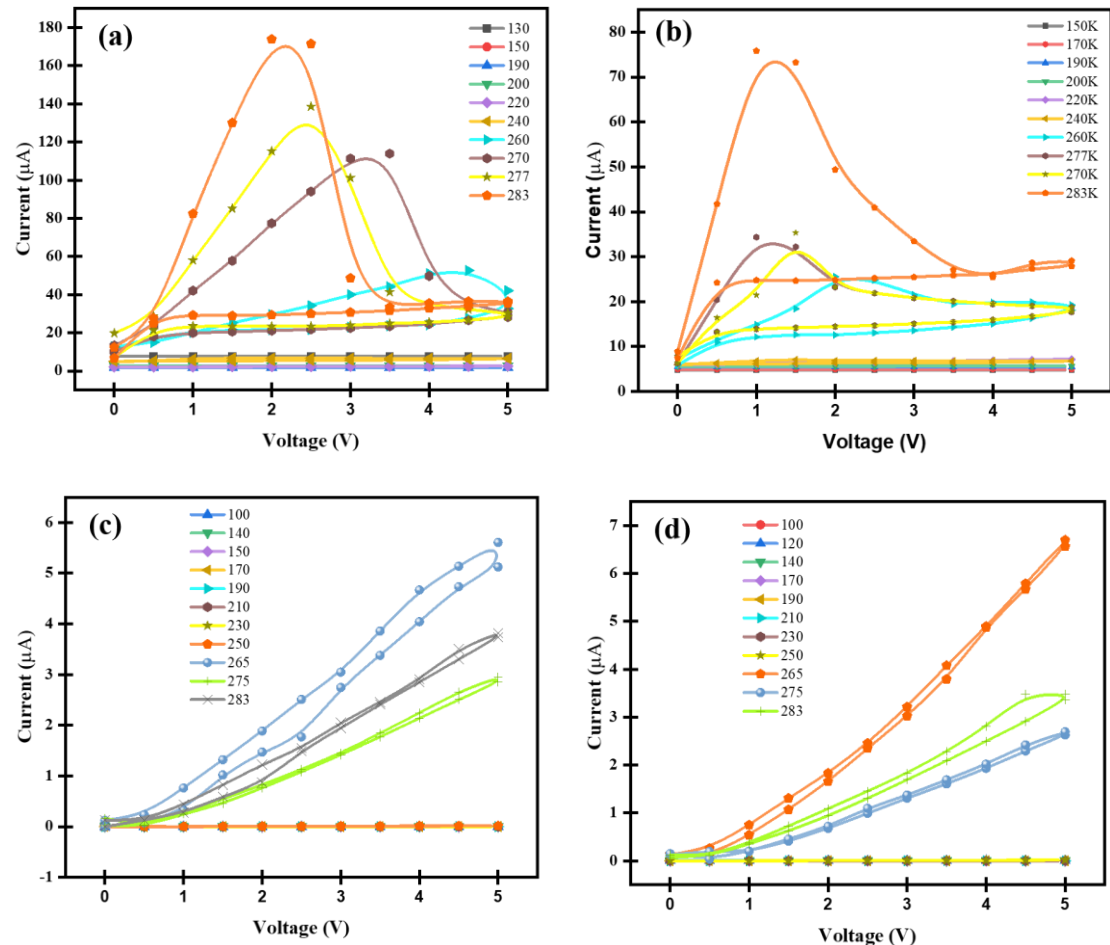
Fig 34. (a), (c) depicts the low temperature, and (b), (d) represent the temperature-dependent I-V (increasing and decreasing from 0 to 5 to 0 V) data for samples with x = 0, 0.33 respectively.

- The exhibition of hysteresis is attributed to the ion migration effect and is confirmed by many past reports.
- Besides, we also observe that at higher temperature the current value exhibits a maximum at a particular voltage and then decreased giving rise to the formation of a peak in the I-V curve.
- The I-V plot for x=0 is demarcated by two distinct regions on either side of a peak maximum at a certain applied bias. This phenomenon may be attributed to ion migration due to external electric field bias.
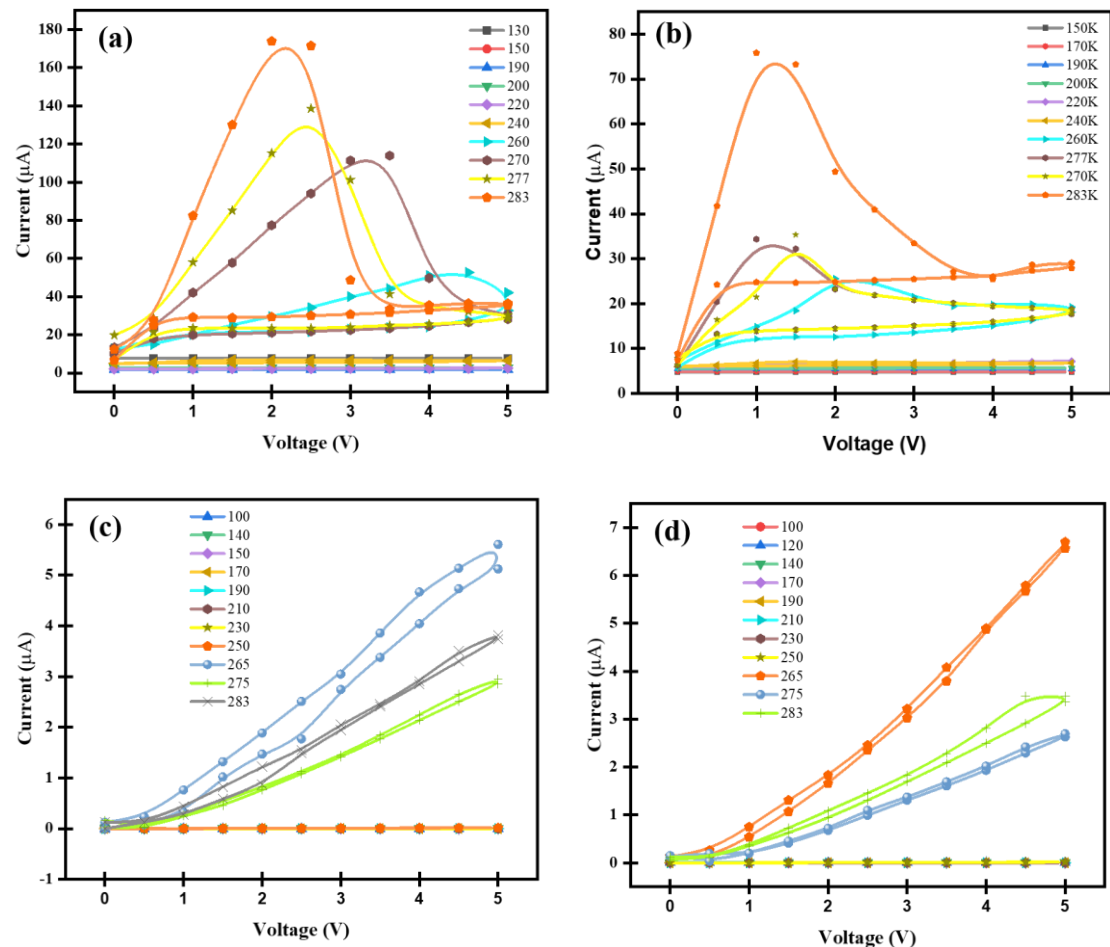
**Fig 34.** (a), (c) depicts the low temperature, and (b), (d) represent the temperature dependent I-V (increasing and decreasing from 0 to 5 to 0 V) data for samples with x = 0, 0.33 respectively.

- On the left side of the peak, increase in current is dominated by flow of electrons due to applied external electric field. As the external field is increased, the ion migration gives rise to a partial phase segregation induces electric field opposite to the applied electric field.
- This plausibly gives rise to a maximum in the I-V plot beyond which the induced field becomes strong enough to reduce the current as can be seen on the right side of the peak.
- When the applied bias is low, the process of ion migration may be reversible, however, after a certain applied field, the ion migration process leads to phase segregation in the sample which eventually becomes an irreversible one.
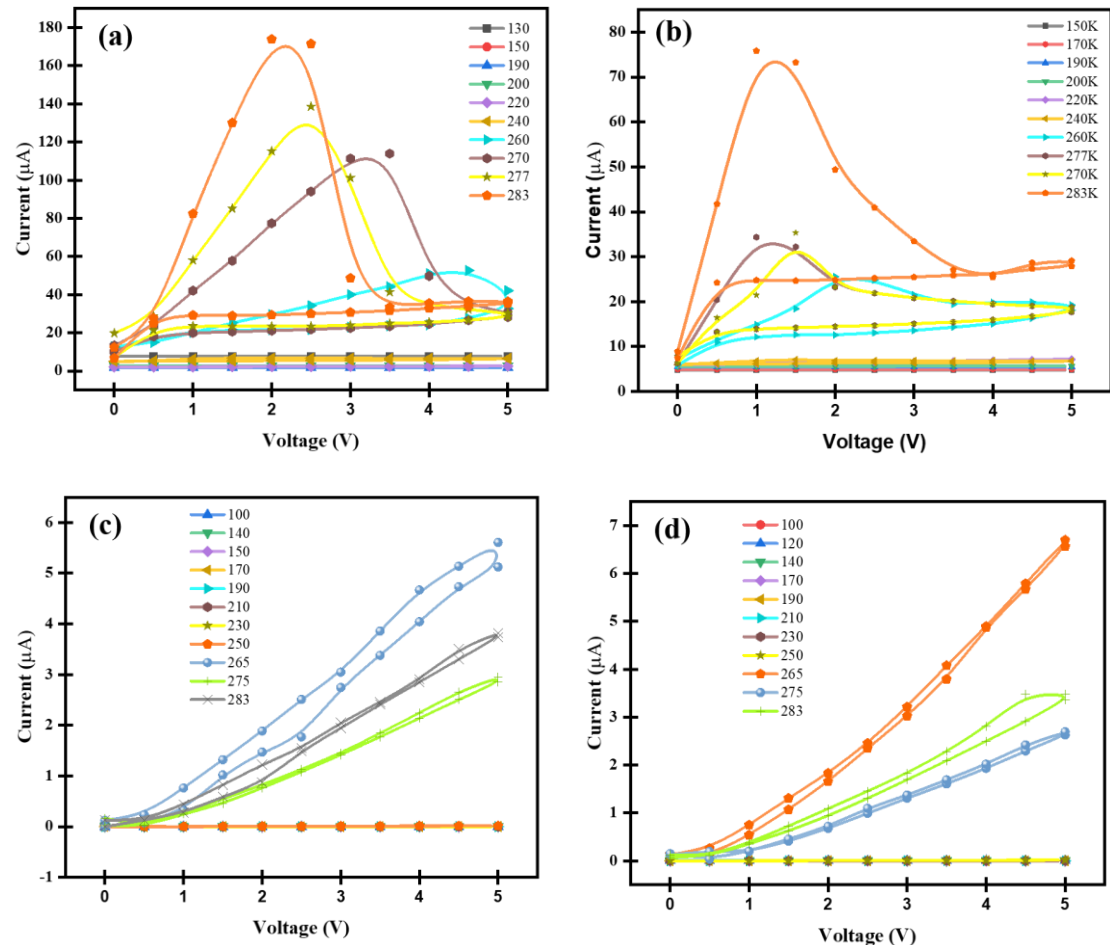
- Consequently, when the scanning cycle is reversed 5 to 0 V, the I-V plot does follow a different path for the growth of current giving rise to a hysteresis effect.
- The above discussion clearly confirms the role of ion migration and phase segregation in controlling the electron transport in perovskite materials which has far-reaching consequences on the stability and efficiency of the solar cell device.
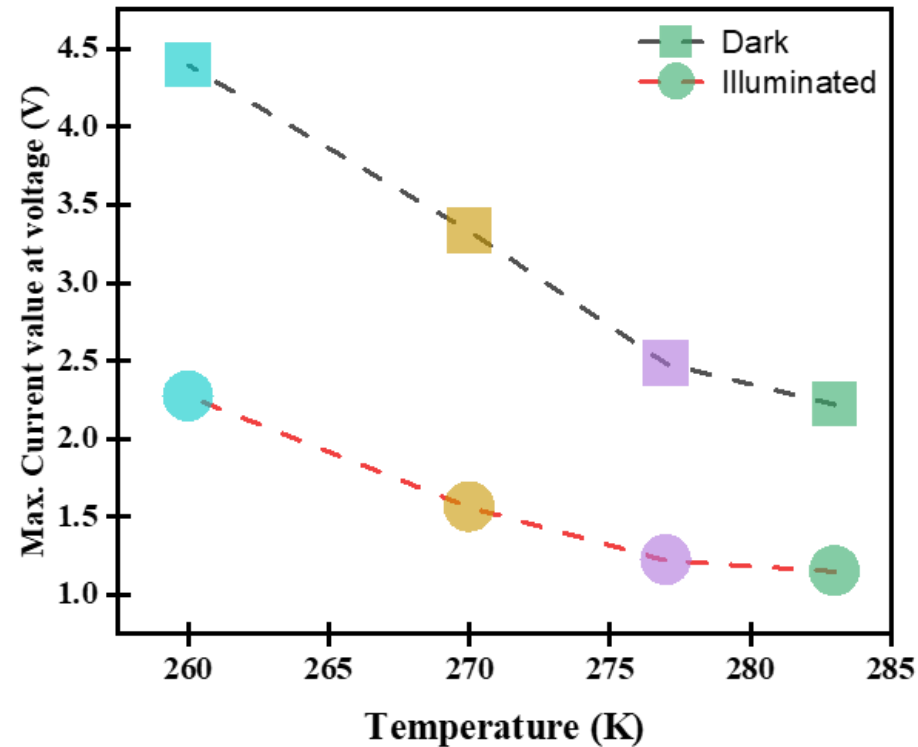
**Fig 34 .** (a), (c) depicts the low temperature, and (b), (d) represent the temperature dependent I–V (increasing and decreasing from 0 to 5 to 0 V) data for samples with x = 0, 0.33 respectively.

**Fig 35.** Maximum current value at voltage vs. temperature plot.

- I-V plot with external photo bias is plotted which shows almost the same hysteresis behaviour.
- With applied photo bias the voltage–temperature curve shifts downward.
- This phenomenon can be explained by the ion migration due to incident photo bias.
- As explained earlier, phase segregation is an accumulative process initiated by ion migration.
- External photo bias increases the number of migrated ions so phase segregation is achieved with low external electric field bias.
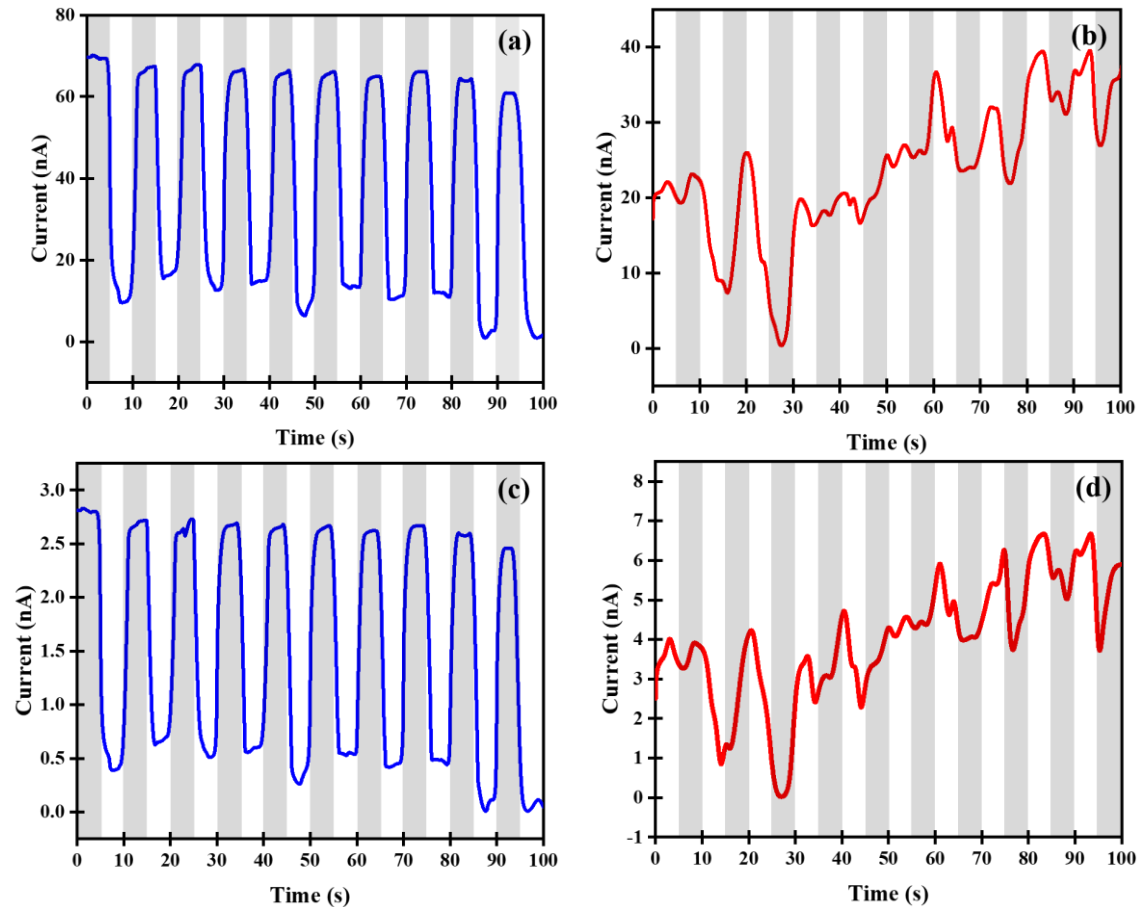
**Fig 36.** (a), (c), (e), (g), (i) depict the low temperature, and (b), (d), (f), (h), (j) depicts the high-temperature I–t data for samples with x = 0, 0.33, 0.0.44, 0.55, 0.66, respectively.

- The NPC phenomenon is observed to be reversible and transient. The reversibility and transient nature of the process suggest that the process is dominated by the effect of ion migration (reversible) without being phase segregated (irreversible).
- Fast ion migration or phase segregation was already reported by Suchan et.al..
- We propose that the nucleation of migrated charges is energetically more favorable when the sample is under illumination.
- The opposing electric field due to ion migration-induced effect leads to the reduction in current, giving rise to the observed negative photoconduction in our samples.
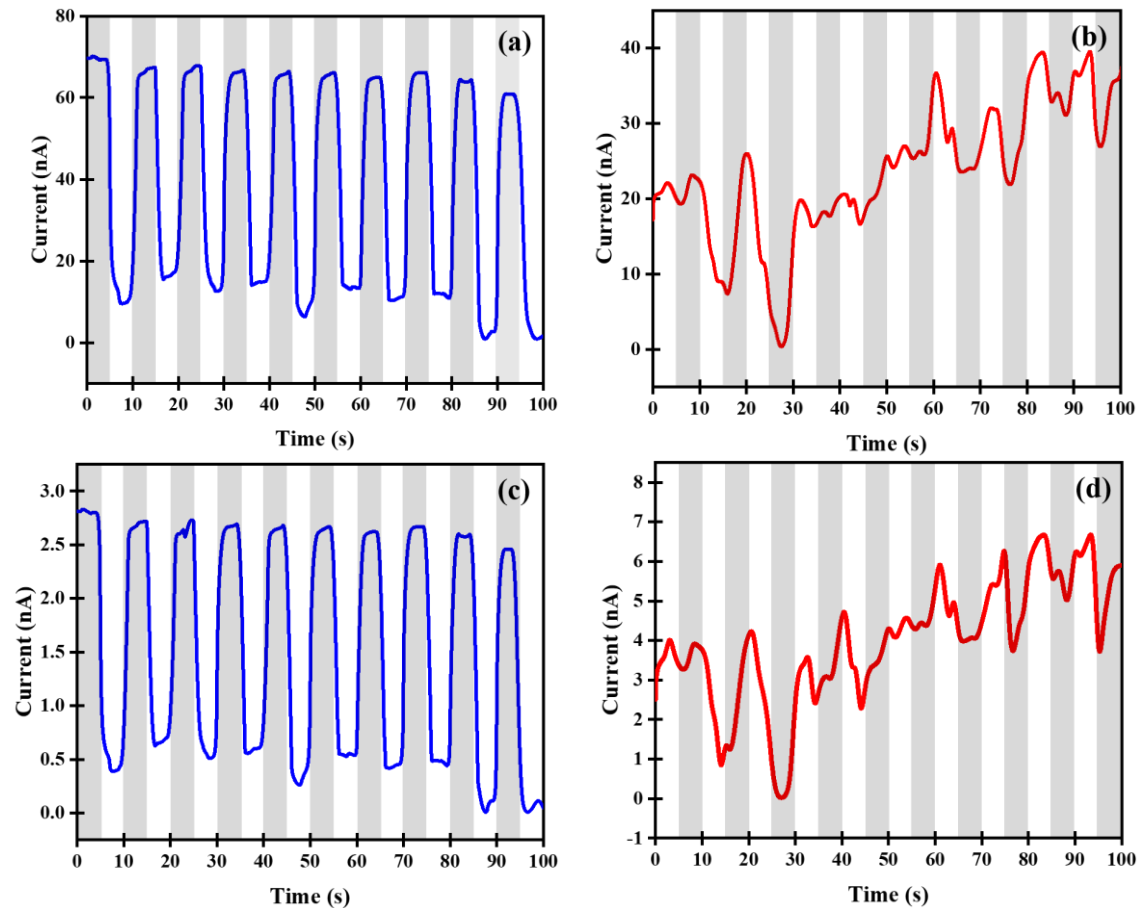
**Fig 36.** (a), (c), (e), (g), (i) depict the low temperature, and (b), (d), (f), (h), (j) depicts the high-temperature I-t data for samples with x = 0, 0.33, 0.0.44, 0.55, 0.66, respectively.

- For x = 0, the case may be explained by the process of ion migration of only halide ions (Cl⁻) under light illumination.

- When the photo bias is applied, migration of halide ions gives rise to a thermodynamically stable configuration and recovers its original position instantly when the photo bias is removed leading to the observed reversibility of the process.

- The scenario changes for a mixed halide perovskite, as the case for our samples MABiBrCl. To be noted that, there is a significant difference in mass (Br is heavier than Cl) and mobility (Cl is more mobile) values for two halide ions Cl⁻ and Br⁻.
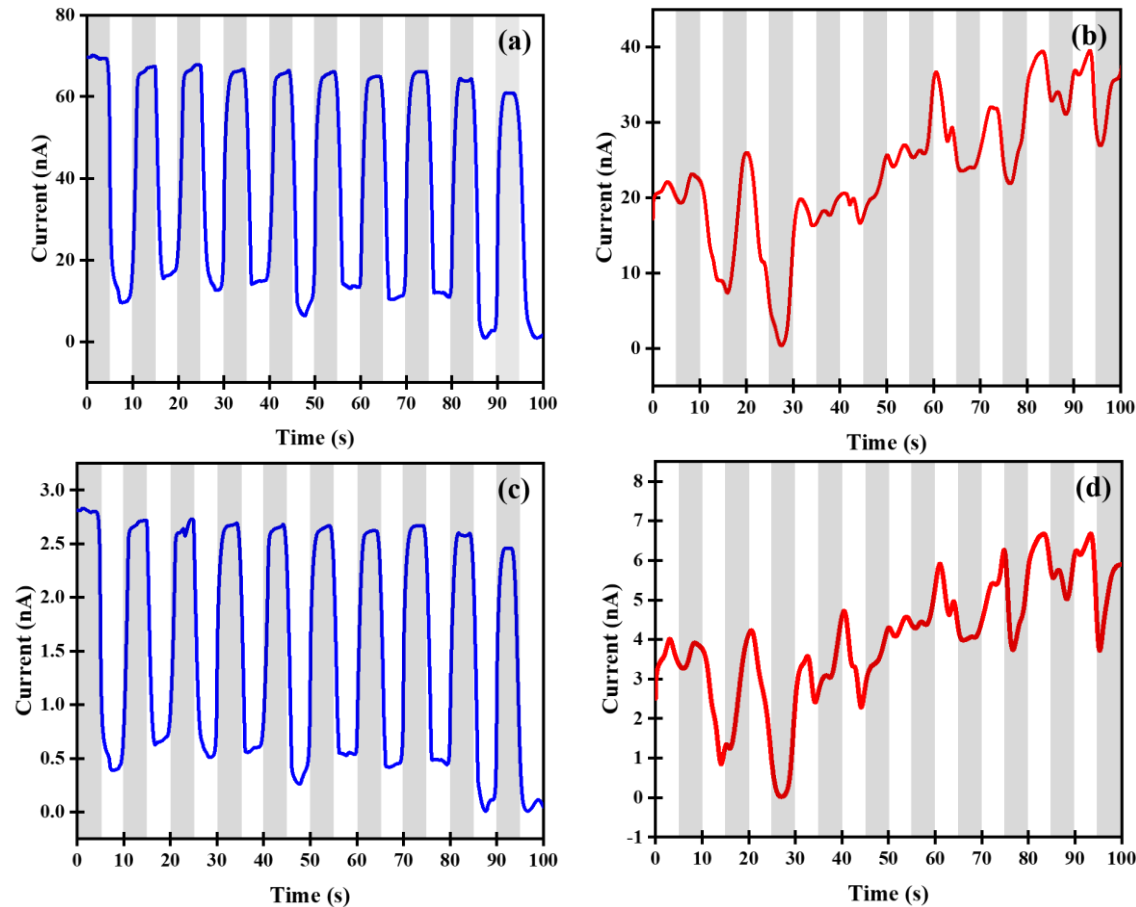
**Fig 36.** (a), (c), (e), (g), (i) depict the low temperature, and (b), (d), (f), (h), (j) depicts the high-temperature I-t data for samples with x = 0, 0.33, 0.0.44, 0.55, 0.66, respectively.

- This, in turn, leads to two different thermodynamical stable states with different energy minimums.
- As the temperature is increased (300 K here), the ions gain sufficient energy giving a more mixed state of halide ion (both Br and Cl) configuration, and the screening effect is reduced.
- Although NPC is less dominant, the process is still reversible and transient.
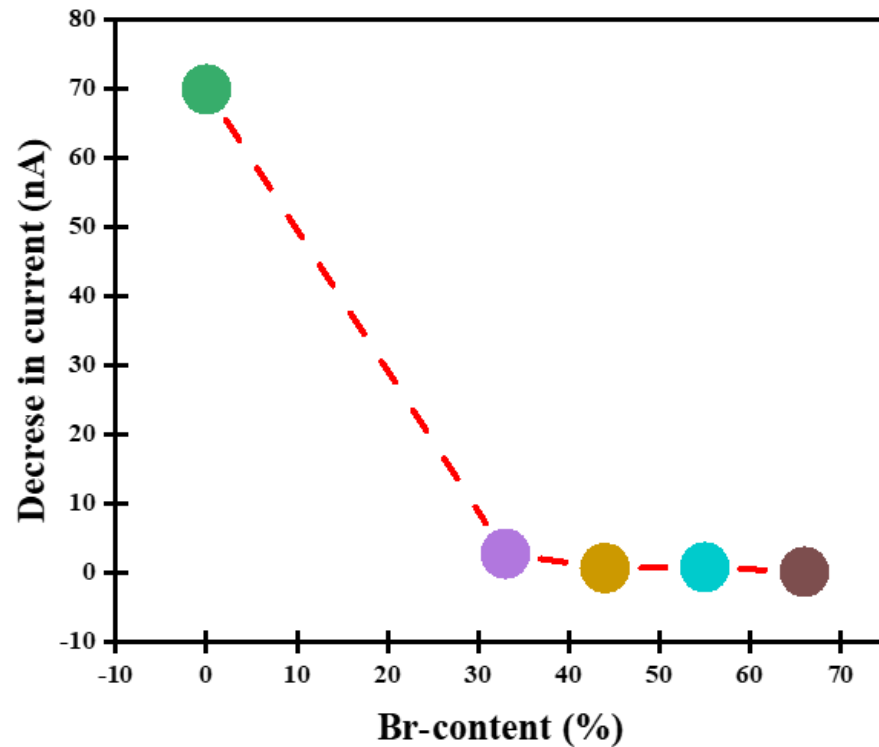
**Fig 37.** Decrease in photo negative current with Br-content

- Now, as the Br concentration increases, the NPC effect gets reduced, as can be seen from the % change in photo-current value from its dark counterpart.
- The presence of two halide ions generates an electric field screening of the opposing electric field and the lesser effect of NPC as the Br/Cl ratio increases.
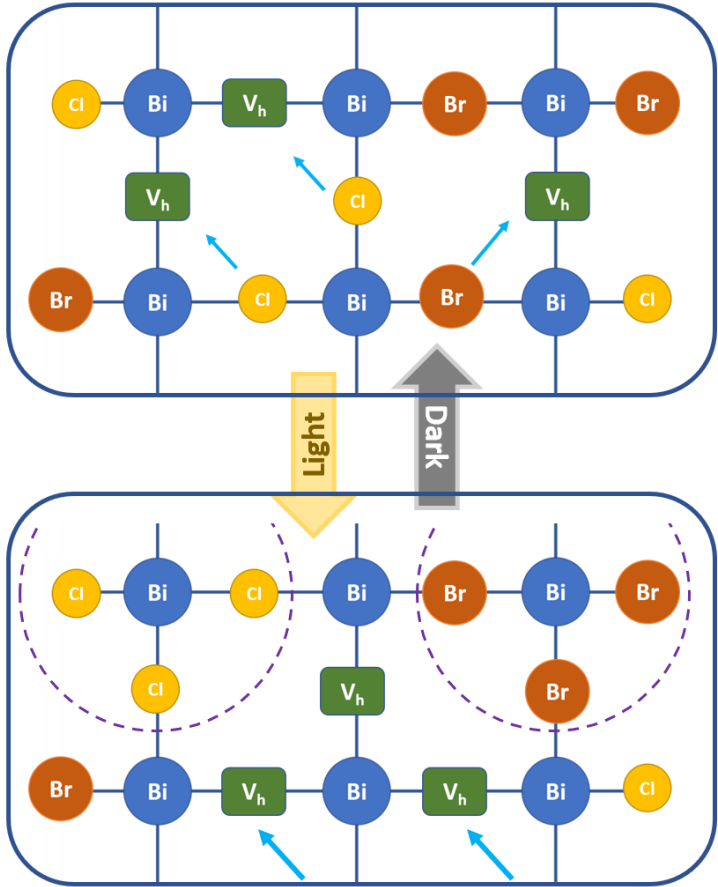
**Fig 38.** Schematic diagram of ion migration

**Fig 39**. Schematic diagram of Bi-based perovskite solar cell
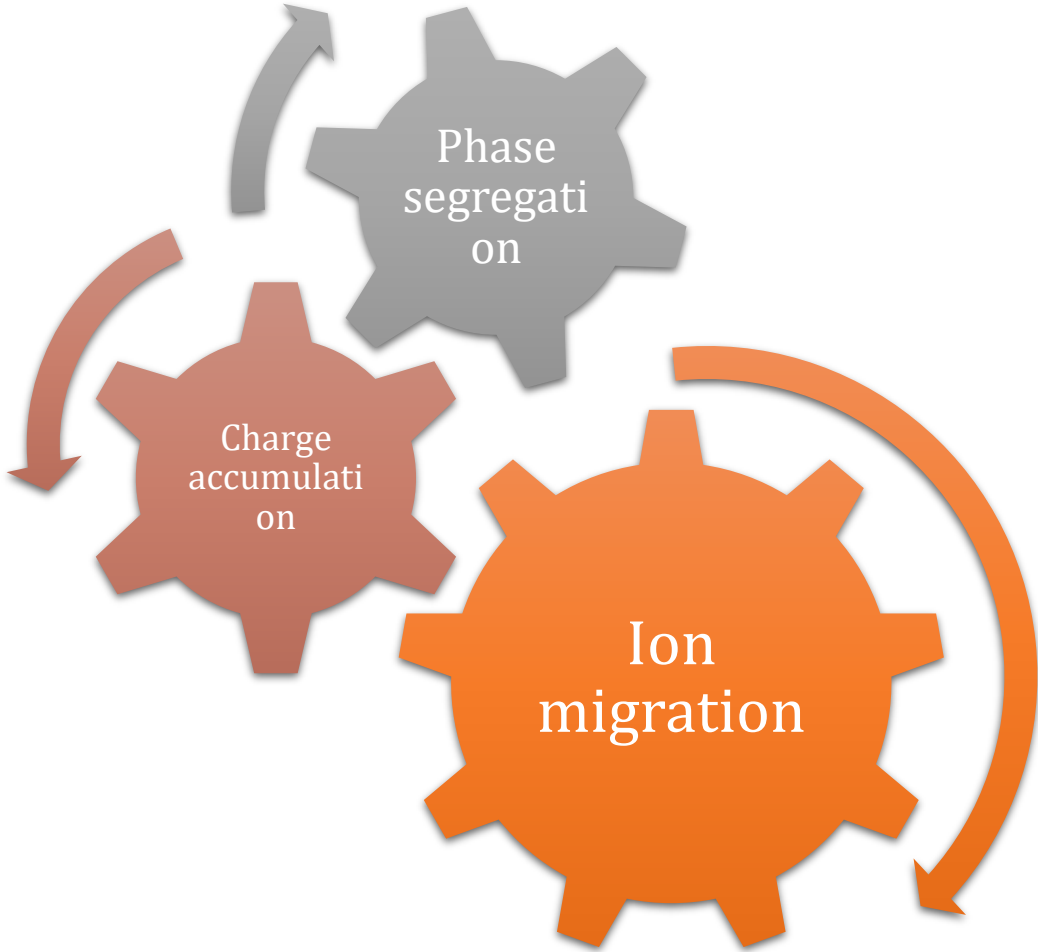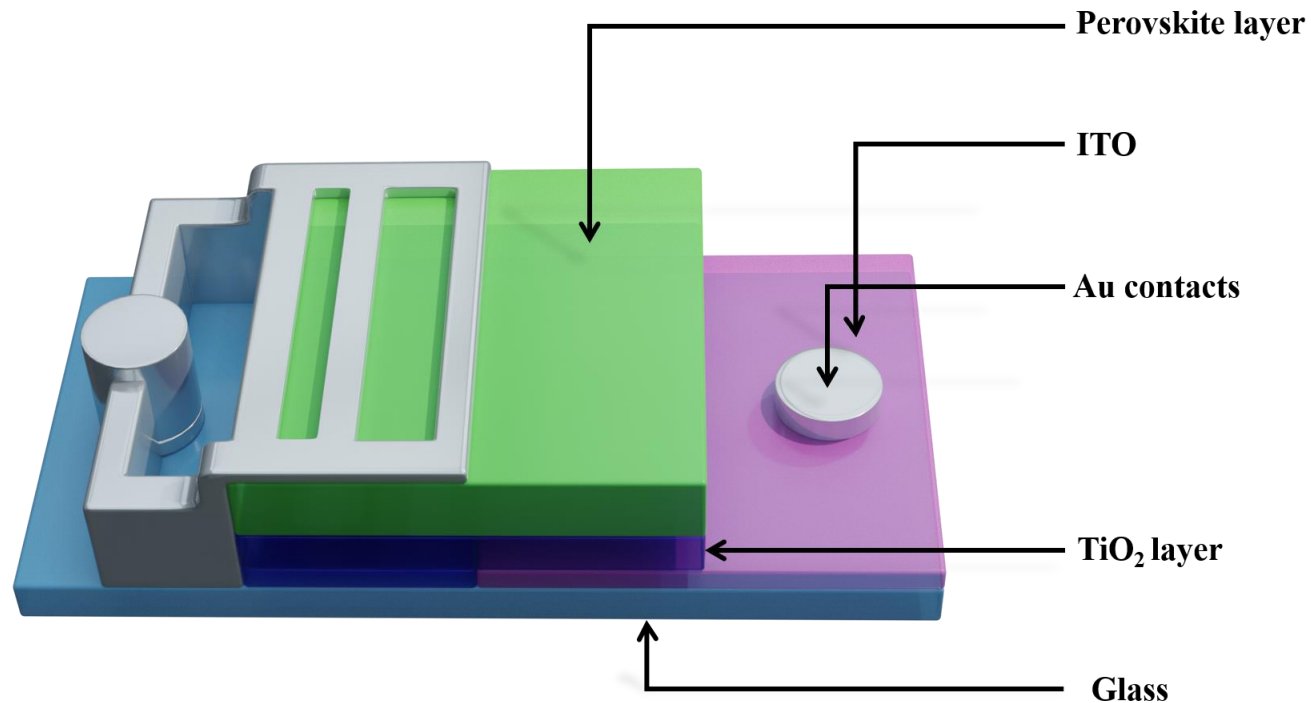
- We have used $MABiBr_{0.44}Cl_{0.55}$ as the absorber layer for perovskite solar cells. The NPC effect is considerably low for the Br-doped samples, and we hoped to get better efficiency with that.

- In fig., a new design for perovskite solar cells is depicted.

Efficiency ($\eta$) = 0.398 %

Open-circuit voltage ($V_{OC}$) = 1.27 V

Fill-factor (FF) = 77.449 %

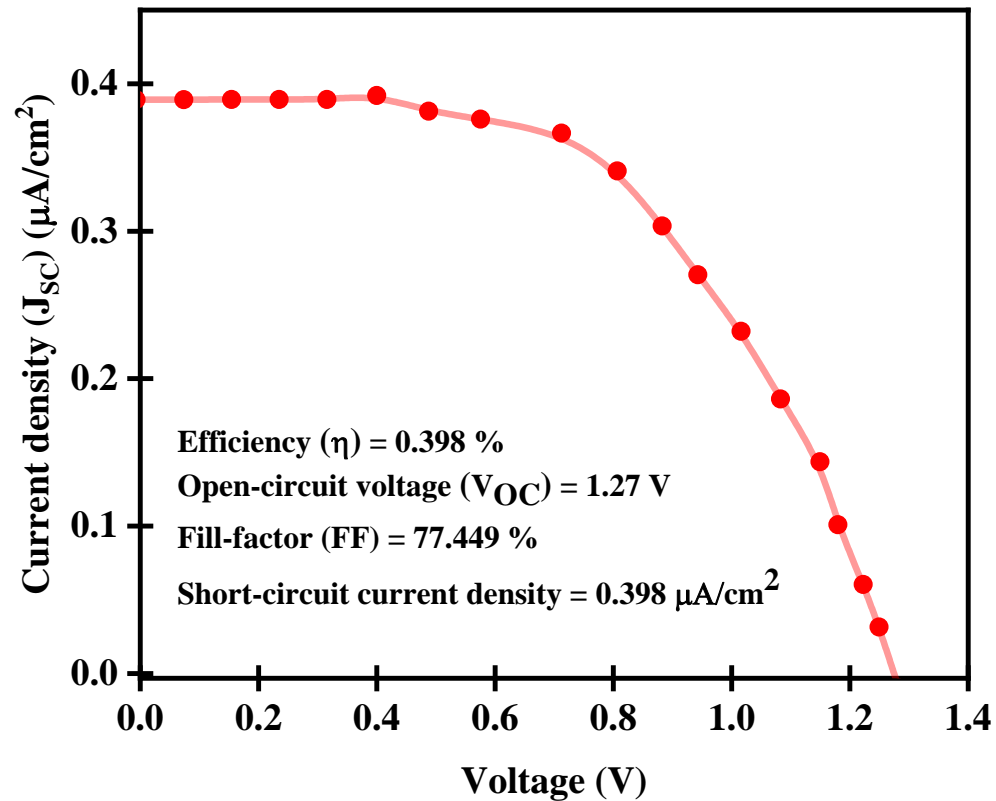Short-circuit current density = 0.398 $\mu A/cm^2$

**Fig 39:** J-V characteristic curve of the ITO/Meso-TiO$_2$/

MABiBrCl/Ag/ITO device.

- **Efficiency = 0.398 %**

- **Open-circuit voltage $V_{OC}$ = 1.27 V**

- **Fill-factor (FF) = 77.449 %**

- **Short-circuit current density $J_{SC}$ = 0.398 $\mu A/cm^2$**

**Fig 40:** J-V characteristic curve of the ITO/Meso-TiO$_2$/ $[(CH_3NH_3)_3Bi_2Cl_9]_n$/Ag/ITO device.
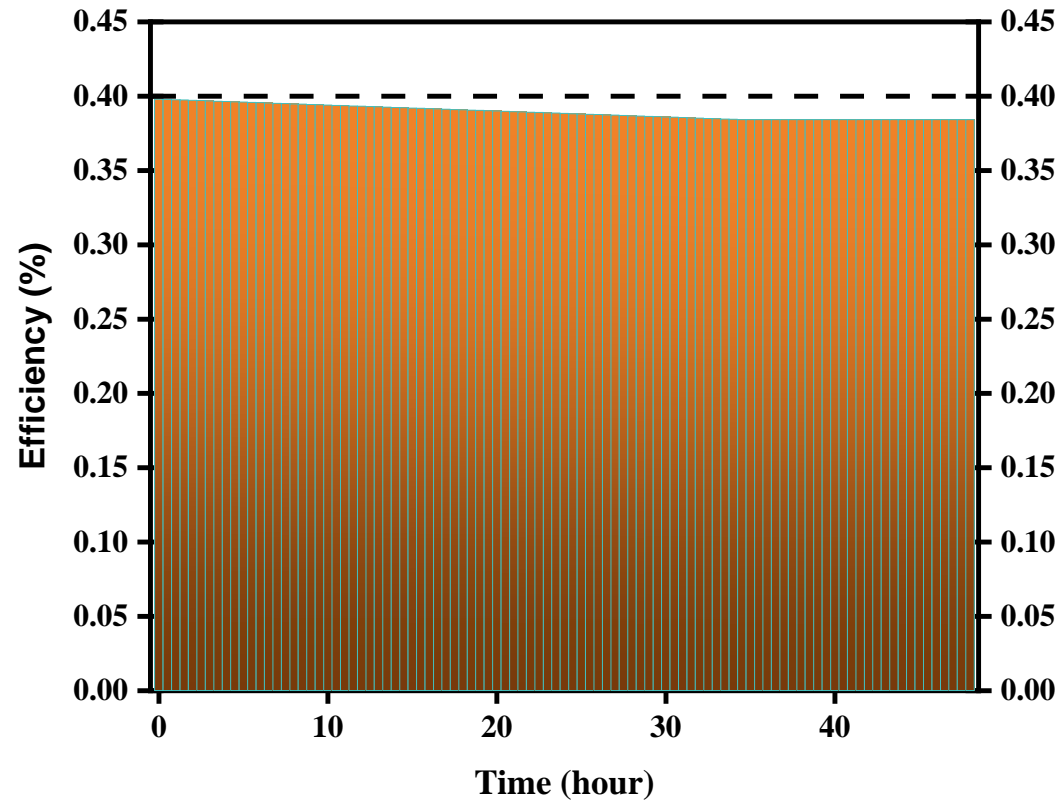
- **Loss in efficiency in 48 hours of constant illumination = 2.412 %**
- **Estimated lifetime = 2000 h**

## Progress so far

# Conclusion

- In summary, we have prepared a perovskite material MABiCl as the light sensitizer layer to fabricate Pb free perovskite solar cell.
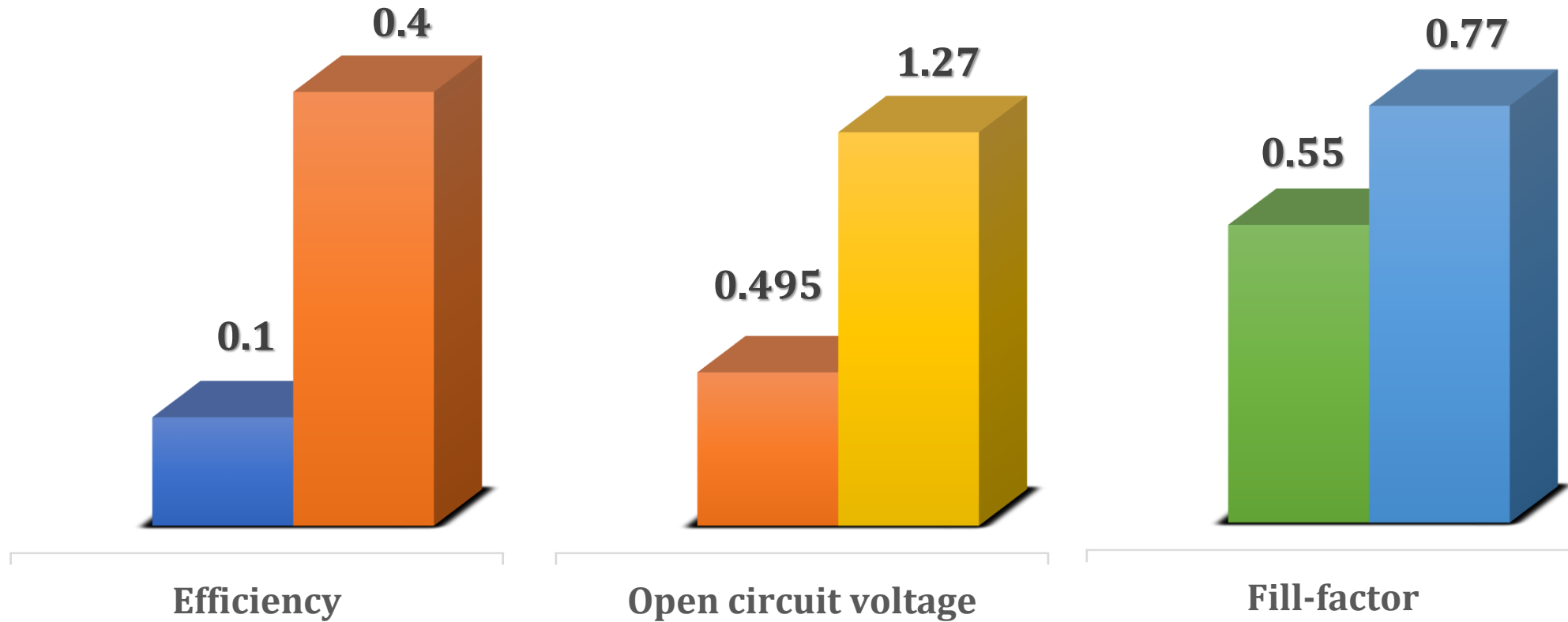
- The synthesis process adopted here facilitates faster evaporation of the solvent and a sequential deposition of the perovskite film on ITO substrate resulting in better surface coverage, morphology and regular distribution of disc-shaped flakes.

- The solar cell device showed a relatively high open-circuit voltage of 496 mV and good fill factor 0.55. Although solar cell efficiency was found to be low <1%, we believe this could be further improved with use of optimized film thickness, more control on surface morphology, and good electrical contacts.

- Moreover, the absorber layer with a bandgap of 2.58 eV and polymeric structure can be used in device applications like photo-detectors, LEDs, batteries, and supercapacitors.

# Conclusion

- Dielectric behaviors of MABiCl and MABiBrCl samples have been reported here.

- Frequency and temperature-dependent electrical transport properties based on dielectric studies reveal complex characteristics of these hybrid perovskite materials.

- The obtained experimental results are further analyzed with theoretical models considering the probable contribution of the electrical contact, grains, and grain boundaries which eventually modified the relaxation of carriers within the perovskite material.

- We also noticed that the activation energy is relatively higher for the Br-doped MABiBrCl than MABiCl, which might explain some of the properties reported on solar cells and optoelectronic devices.

# Conclusion

- Dielectric behaviours of MABiCl and MABiBrCl samples at 100-300 K are reported here.

- We observed that the crystallinity of the samples was largely unaffected by doping.

- The dielectric studies indicated a sharp change in permittivity at a particular critical temperature of 270 K and 266 K for MABiCl and MABiBrCl, respectively.

- This can be related to a change in the orientation of the MA ions giving rise to a structural phase transition which is dependent on temperature.

- The studies performed here agree with the proposed model in which the rotational motion of MA ions around the C-N axis and its temperature dependence were considered.

# Conclusion

- We can clearly infer that the NPC and halide migration phenomenon is related to each other.

- Also, there are two kinds of phenomenon with different time scales present. The NPC phenomenon can be primarily described by the fast creation of shallow, transient states in the presence of light, and current hysteresis is depicted as slow phase segregation of the system.

- Presumably, we can also quantify the halide segregation effect using the NPC effect, as the electrical measurement for NPC is easy to access. Previous studies to identify the halide and phase segregation mainly concentrated on photoluminescence studies or more sophisticated PL-mapping study. We propose an alternative to measuring the halide segregation phenomenon by the electrical route.

- The dependence of Br doping is also observed, which helps to suppress both the NPC and halide segregation effects.

- The presence of two halide ions drastically improves the situation. In previous works of lead-based solar cells, the Br-doped counterpart of the perovskite structure is more suited and stable. This fact can be rationalized by the halide migration and phase segregation we observed due to the presence of two halide ion species with different mobility.

# Conclusion

- Also, to emphasize the importance of halide migration detection, we turn toward the perovskite solar cell performance. Ion migration is a major issue to tackle concerning perovskite solar cell degradation.

- We also observed that the NPC effect is fast and mostly reversible in low temperatures, which can find good use in ultrafast photodetectors.

- We have used Br doped perovskite sample (x = 4) as the absorber layer and observed the highest efficiency of 0.398 %, FF = 77%, $V_{OC}$ = 1.4 V, and the cell are stable (with lifetime 2000 h).

# Arrangement of Thesis

- **Chapter 1:** Introduction and literature survey

- **Chapter 2:** Methods and Instrumentation

- **Chapter 3:** Morphology controlled $(CH_3NH_3)_3Bi_2Cl_9$ thin film for lead free perovskite solar cell

- **Chapter 4:** A dielectric study of Br-doped lead-free methylammonium bismuth chloride

    $(CH_3NH_3)_3Bi_2Br_xCl_{9-x}$

- **Chapter 5:** Frequency and temperature dependent dielectric characteristics of lead free Br doped

    perovskite $(CH_3NH_3)_3Bi_2Cl_9$ and $(CH_3NH_3)_3Bi_2Br_xCl_{9-x}$

- **Chapter 6:** Observation of negative photoconductivity in $(CH_3NH_3)_3Bi_2(Br_xCl_{1-x})_9$: correlating ion-

    migration, instability and efficiency in halide perovskite solar cell

- **Chapter 7:** Conclusions

- **References**

- **Future works**

- We are currently studying the Bi-based perovskite stability. The instrument we have developed to study the effect of different biasing conditions will be upgraded, and the Python-based interface will be translated to a LabVIEW-type interface with proper UI.

- The instrument we have developed will also be employed to study the fundamental properties of other kinds of materials. Proper modifications of the software and external stimuli will be conducted.

- We plan to employ dielectric spectroscopy measurement on the entirely fabricated device to explore the interface contribution to solar cell performance.

- Some drift diffusion-based simulation software (like SCAPS-1D) will be used to find the best possible device configuration.

- We are also interested in exploring negative photoconductivity-based ultrafast photodetectors.

**As first author**

1. **P. Chandra**, S.K. Mandal, Morphology controlled $(CH_3NH_3)_3Bi_2Cl_9$ thin film for lead free perovskite solar cell, Physica B: Condensed Matter. 625 (2021) 413536. https://doi.org/10.1016/j.physb.2021.413536.

2. **P. Chandra**, S. Saha, S.K. Mandal, A dielectric study of Br-doped lead-free methylammonium bismuth chloride $(CH_3NH_3)_3Bi_2Br_xCl_{9-x}$, Appl. Phys. A. 128 (2022) 541. https://doi.org/10.1007/s00339-022-05677-9.

3. **P. Chandra**, S. Saha, S.K. Mandal, Frequency and temperature-dependent dielectric characteristics of lead-free Br doped perovskites $(CH_3NH_3)_3Bi_2Cl_9$ and $(CH_3NH_3)_3Bi_2Br_xCl_{9-x}$, Materials Today: Proceedings. 66 (2022) 3302–3306. https://doi.org/10.1016/j.matpr.2022.06.413.

4. **P. Chandra**, S.K. Mandal, Observation of negative photoconductivity in $(CH_3NH_3)_3Bi_2(Br_xCl_{1-x})_9$: correlating ion-migration, instability and efficiency in halide perovskite solar cell. (in preparation)

**As a co-author**

1. S. Saha, **P. Chandra**, S.K. Mandal, Spin state bistability in (Mn, Zn) doped Fe(phen)$_2$(NCS)$_2$ molecular thin film nanocrystals on quartz, Physica B: Condensed Matter. 642 (2022) 414128. https://doi.org/10.1016/j.physb.2022.414128.
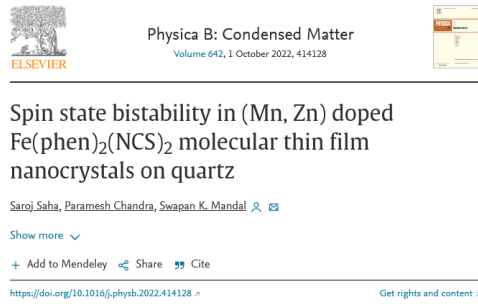
# Acknowledgment

- I express my deep gratitude, regard, and appreciation to my supervisor, Dr. Swapan Kumar Mandal, for his constant encouragement and valuable suggestions. I would have made no progress without his help and support.

- I am really grateful to my family for their constant support and encouragement.

- I would like to thank Arani Chakrabarty and Raj Kumar Singha for their suggestion and help with experiments and instrumentations.

- I thank my lab mates Saroj Saha, Chaitali Mondal, Sujit Rajak, Sampad Mandal, and Dibyendu Majhee for their assistance in different ways.

- Also, I sincerely thank the Head of the Department of Physics and all the faculty members, research scholars, and other staff members of our department for their sincere cooperation during the entire period.

*Thanks for giving me the place to work and identify with.*